Title

Cryo-EM structures of hIAPP fibrils seeded by patient-extracted fibrils reveal new polymorphs and conserved fibril cores.

Journal

Nature Structural and Molecular Biology, 28(9)

Authors

Cao, Qin
Boyer, David
Sawaya, Michael
et al.

Publication Date

2021-09-01

DOI

10.1038/s41594-021-00646-x

Peer reviewed

Published in final edited form as:

Nat Struct Mol Biol. 2021 September ; 28(9): 724–730. doi:10.1038/s41594-021-00646-x.

Cryo-EM structures of hIAPP fibrils seeded by patient-extracted fibrils reveal new polymorphs and conserved fibril cores

Qin Cao[1,2], **David R. Boyer**[1], **Michael R. Sawaya**[1], **Romany Abskharon**[1], **Lorena Saelices**[1,3], **Binh A. Nguyen**[1,3], **Jiahui Lu**[1], **Kevin A. Murray**[1], **Fouad Kandeel**[4], **David S. Eisenberg**[1,*]

[1]Department of Chemistry and Biochemistry and Biological Chemistry, UCLA-DOE Institute, Molecular Biology Institute, and Howard Hughes Medical Institute, UCLA, Los Angeles, CA, USA.

[2]Current address: Bio-X Institutes, Key Laboratory for the Genetics of Developmental and Neuropsychiatric Disorders, Ministry of Education, Shanghai Jiao Tong University, Shanghai, China.

[3]Current address: Center for Alzheimer's and Neurodegenerative Diseases, Department of Biophysics, UT Southwestern Medical Center, Dallas, TX, USA.

[4]Department of Translational Research & Cellular Therapeutics, City of Hope, Duarte, CA, USA.

Abstract

Amyloidosis of human islet amyloid polypeptide (hIAPP) is a pathological hallmark of type II diabetes (T2D), an epidemic afflicting nearly 10% of the world's population. To visualize disease-relevant hIAPP fibrils, we extracted amyloid fibrils from islet cells of a T2D donor and amplified their quantity by seeding synthetic hIAPP. Cryo-EM studies revealed four fibril polymorphic atomic structures. Their resemblance to four unseeded hIAPP fibrils varies from nearly identical (TW3) to non-existent (TW2). The diverse repertoire of hIAPP polymorphs appears to arise from three distinct protofilament cores entwined in different combinations. The structural distinctiveness of TW1, TW2, and TW4 suggests they may be faithful replications of the pathogenic seeds. If so, the structures determined here provide the most direct view yet of hIAPP amyloid fibrils formed during T2D.

*Correspondence to : David S. Eisenberg, david@mbi.ucla.edu.

Author contributions:

Q.C. designed experiments and performed data analysis. F.K. prepared islet cells from donors. Q.C. and L.S. performed Congo red staining of islet cells. Q.C., L.S., and B.A.N. performed fibril extraction from islet cells. Q.C. and R.A. performed immunoprecipitation in fibril extraction. R.A. and J.L. performed western blot and MTT assays. K.A.M. helped in western blot. Q.C. prepared hIAPP fibrils and cryo-EM grids. Q.C. and D.R.B. collected cryo-EM data. Q.C. performed cryo-EM data processing and model building, J.L. assisted in particle picking. Q.C. and M.R.S. performed solvation energy calculation. All authors analyzed the results and wrote the manuscript. D.S.E. supervised and guided the project.

Competing interests:

D.S.E. is an advisor and equity shareholder in ADRx, Inc. The remaining authors declare no competing interests.

Code availability

Energetic calculations were performed using custom written software, and the code is available at MBI website (URL: https://people.mbi.ucla.edu/sawaya/amyloidatlas/accessiblesurfacearea_v07.2d.f)

Introduction

The tissue deposition of amyloid fibrils is a hallmark of the amyloid family of diseases, including Alzheimer's, Parkinson's, and T2D. These fibrils are associated with, and possibly causal of disease[1]. Associated with T2D are fibrils of hIAPP (or amylin), a human protein hormone of 37 residues, which works with insulin to regulate blood sugar levels[2,3]. Pancreatic amyloid deposits of hIAPP are found in more than 90% of T2D patients[4–6], and genetic and experimental evidences link them to the pathogenic mechanism of T2D[7–11]. Accordingly, determining the near-atomic resolution structures of these disease-related hIAPP fibrils may help to understand the molecular mechanism of pathogenesis of T2D, and can offer essential information for structure-based design of inhibitors of amyloidosis.

Our previous cryo-EM study revealed the structure of amyloid fibrils formed by full-length recombinant hIAPP fused to a SUMO-tag[12], adding to the collection of models and near-atomic resolution structures reported for fibrils of synthetic and un-tagged hIAPP peptide[13–16]. Whereas these structures were all obtained from hIAPP fibrils formed in vitro, recent studies on tau and α-synuclein suggest that in vitro fibrils may not adopt the same structures as patient-extracted fibrils[17,18]. These findings raise the question of whether the reported hIAPP fibril structures are disease related. Here, we extracted hIAPP fibrils from islet cells of a donor with T2D to seed the fibril formation of synthetic hIAPP, and determined four cryo-EM structures from seeded fibrils, with the expectation that the seeded fibrils may replicate the structure of the seeds (Supplementary Text 1).

Results

T2D patient fibrils seed fibrilization of synthetic hIAPP

We extracted hIAPP fibrils from the islet cells of a donor with T2D, and used these extracted fibrils to seed the fibril formation of synthetic hIAPP peptides. We first tested the amyloid content in islet cells from 7 donors with T2D (Case 1 to Case 7) by Congo red staining. Samples from one donor (Case 6) exhibited strong Congo red staining while samples from two other donors (Case 4 and Case 5) exhibited medium staining (Fig. 1A, Extended Data Fig. 1A, and Supplementary Table 1). We selected Case 6 for further study. Genotyping revealed that the hIAPP encoded was wild type. We then performed fibril extraction from islet cells of Case 6 by following the protocol reported previously and combined with immunoprecipitation (see Methods). Our goal is to determine the structure of T2D-relevant hIAPP fibrils. However, patient extracted fibrils are too scarce for cryo-EM study. To amplify the quantity of sample, we used the patient-extracted fibrils to seed synthetic hIAPP, generating abundant, long fibrils for cryo-EM determination (Fig. 1 and Extended Data Fig. 1, see Methods for detail).

Cryo-EM structures of seeded hIAPP fibrils

We identified 8 different morphologies during 2D classification: four were clearly twisted (termed TW1-4) and suitable for structure determination and four were not twisted (termed NT1-4, Fig 2, Extended Data Fig. 2A&B). TW1 is the most abundant species and contains about 30% of all identifiable segments, whereas TW2, TW3 and TW4 contain 15%, 10%

and 10%, respectively. NT1-4 together account for the remaining 35% of particles but their lack of twisting precludes 3D structure determination. We determined the cryo-EM structures of TW1 to TW4, with resolution ranging from 3.8 to 4.1 Å (Fig. 2, Extended Data Fig. 2C–E, Extended Data Fig. 3, and Table 1). These structures displayed the typical cross-β scaffold of amyloid fibrils, consisting of layers of β-strands stacked with a 4.8 Å spacing (Fig. 2 and Extended Data Fig. 3).

All four fibril polymorphs are composed of two intertwined chains or protofilaments. The two protofilaments are related by a C_2 symmetry axis in the TW2 fibrils and by a pseudo-$P2_1$ axis in TW3 fibrils. In TW1 and TW4, which we term heterotypic fibrils, the two protofilaments (chains A and B) are conformationally distinct from each other (Fig. 2 and Extended Data Fig. 4A).

We note that at the current resolution (3.7 to 4.1 Å) cryo-EM refinement usually suffers from local minima problems[19], which may raise the risk of incorrect map and/or model. However, we were able to build unambiguous models based on map fitting as well as external information, such as cross-validation via other structures and determining the terminus of the main chain (see Methods for detail).

In the final models, we observed density for the C-terminal residue of hIAPP (Tyr37) in all chains except for TW4 chain B (Extended Data Fig. 5A). The lack of additional density beyond Tyr37 in all polymorphs except TW4 chain B and the lack of space for building additional residues beyond Tyr37 in TW2, TW3, and TW4 chain A supports the registration of the models into the maps (Extended Data Fig. 2C and Extended Data Fig. 5B&C). Furthermore, the finding that the amide moiety of Tyr37 forms a hydrogen bond to stabilize the fibril fold on TW2, TW3 and TW4 chain A is consistent with the previous observation that C-terminal amidation promotes amyloidosis of hIAPP[20] (Extended Data Fig. 5C). Density for the N-terminal region was more variable; the first ordered residue differs among polymorphs from Thr6 (in TW2 and TW4 chain A) to Val17 (TW1 chain B, Extended Data Fig. 5A). In TW2-4, we found extra density near the N-terminus, suggesting the position of additional N-terminal residues (Fig. 2 and Extended Data Fig. 5B, see Discussion).

Three seeded polymorphs are previously unreported forms

Three of the four seeded hIAPP fibril structures are distinct from previously reported un-seeded ones. We consider fibrils 6Y1A[15] and 6ZRF[16] as un-seeded controls of our study given that in all three studies identical starting material – C-terminally amidated hIAPP – and similar fibril growth conditions were used. Those two un-seeded control studies revealed fibril structures similar to each other (disregarding opposite assignment of fibril handedness, Fig. 4B, see Methods for detail) as the dominant species (90% and 80% of total fibril populations, respectively). In our seeded experiment, we found one species, TW3, matches the dominant conformation of 6Y1A and 6ZRF (Extended Data Fig. 4B), but it contributes only 10% of the total population. The majority of the seeded fibrils are polymorphs TW1, TW2 and TW4, whose structures differ from the unseeded controls.

Structural alignment at the protofilament level

We selected all unique hIAPP conformations (a single layer in a protofilament in a fibril) among all reported hIAPP fibril structures (Table 2) and performed pairwise structural alignment (see Methods). We found all conformations except TW2 can be categorized into two groups: Core Fold 1 (CF1) and Core Fold 2 (CF2, Fig. 3A &B, see Supplementary Text 2). Unlike the other structures, TW2 is composed of unique protofilament folds as evidenced by the superposition with TW1 chain A and chain B (Extended Data Fig. 4D). In the following, we refer to the fold of TW2 as Core Fold 3 (CF3).

CF1 and CF2 form different protofilament interfaces

The two core folds (CF1, CF2) we observe in most hIAPP fibril structures can be combined in three different ways to form a fibril. All three have been observed, including the two homotypic types CF1-CF1 (TW1, 6Y1A, and 6ZRF) and CF2-CF2 (6ZRR, 6ZRQ, and 6VW2), and the heterotypic type, CF1-CF2 (TW1, TW4, and 6ZRR, Fig. 3B). The interfaces at which the different protofilaments meet are not conserved; for example, when aligned at CF2 (chain B of TW1, TW4 and 6ZRR), we found the other chains from these three structures are not aligned (Fig. 3C). We examined all significant interfaces of protofilaments presented in hIAPP fibril structures (Extended Data Fig. 5F), and we found all these interfaces are different (see Supplementary Text 3), suggesting that polymorphism arises at the level of protofilament assembly into fibrils.

Comparison of wild-type and S20G hIAPP fibril structures

S20G of hIAPP is the only hereditary mutation so far found in T2D patients, and it was reported to increase the amyloidosis of hIAPP and cause early onset of T2D[21–24]. Structures of hIAPP fibrils containing the S20G mutation have been determined and deposited in the PDB with codes 6ZRR and 6ZRQ[16]. In contrast, the genotype of the patient sample of our study identifies the seeds as wild-type hIAPP, and seeded synthetic monomeric hIAPP we used is also wild-type. Comparison of the S20G structures with the wild-type structures reveals that S20G structures exhibit the same conserved kernels, CF1 and CF2, as the wild-type structures (Fig. 3B). These observations suggest that the S20G mutation enhances fibrilization not by creating new core folds, but instead by favoring the same folds exhibited by wild-type hIAPP.

To improve our understanding of the mechanism by which S20G stabilizes hIAPP fibril structures, we marked position 20 on hIAPP structures with arrows (Fig. 3B), and found that all are located at or near sharp kinks in the main chain. Since the glycine residue is more permissive of a kinked conformation, we suggest the S20G hereditary mutation promotes amyloid formation by allowing the peptide chain more easily to adopt a fibril forming fold.

In addition to favoring a kinked conformation in the main chain, we found another mechanism by which S20G may favor CF2 over CF1 and CF3. We found that among all hIAPP protofilaments that contain CF2, the backbone phi angle at position 20 is positive; whereas the phi angle of position 20 in all other protofilaments is negative (Fig. 3D). Positive phi angles are favored by glycine more than any of the other 19 amino acid residues because only glycine lacks a side chain larger than hydrogen which would

otherwise clash with the main chain in this conformation. This observation suggests that S20G relieves the steric clash among protofilaments that contain CF2, permitting their formation. This hypothesis is supported by the observation that protofilaments with CF2 are more abundant in the S20G fibril dataset compared to wild-type datasets with the exception of 6VW2 (Extended Data Fig. 7A). We note in the 6VW2 dataset that the fibrils are formed by SUMO-tagged recombinant hIAPP without C-terminal amidation, differing from the synthetic and un-tagged hIAPP used in the studies of 6Y1A, 6ZRR and 6ZRQ[15,16]. So perhaps the existence of SUMO-tag and/or the lack of C-terminal amidation drives the fibrils in 6VW2 to the S20G favored CF2 conformation.

Structural similarity of hIAPP and Aβ fibrils

A clinical link between T2D and AD has been reported[25–27] and evidence suggests this link arises from the cross-seeding between hIAPP and Aβ fibrils in patients[28–32]. Cross-seeding is hypothesized to depend on structural similarity between fibrils of hIAPP and Aβ. Previous structural comparisons between hIAPP and Aβ fibrils have supported this hypothesis[12,15,16]. Here, we perform comparisons taking special note of the conserved core folds (CF1 and CF2). These cores, CF1 (residues 15–28) and CF2 (residues 20–33), each cover the region of maximal sequence similarity between hIAPP (19–29) and Aβ (24–34) (Fig. 3E), raising the question of whether analogous structural cores also exist in Aβ. Here we use TW1 chain A and chain B to represent protofilaments with CF1 and CF2, respectively, and together with TW2 (CF3) we compare them with all available Aβ fibril structures. We confined our superpositions to the residue ranges exhibiting maximal sequence identity as noted above (Supplementary Table 3, see Methods for details). The comparisons reveal that each hIAPP core fold exhibits an r.m.s.d under 1.8 Å with some Aβ fibril structure. The best Aβ matches for each of the three groups of hIAPP protofilaments are as follows: 6OIZ with TW1 chain A, 2M4J with TW1 chain B, and 5OQV and 6SHS with TW2 (Fig. 3E). These results suggest that hIAPP and Aβ may be able to cross-seed each other through these regions of sequence and structural similarity.

Discussion

Do our hIAPP structures recapitulate T2D patient seeds?

In this study we determined cryo-EM structures of four hIAPP polymorphs from fibrils seeded by patient-extracted seeds. Our structure TW3 is similar to 6Y1A[15] and 6ZRF[16] from un-seeded controls; our structures TW1, TW2 and TW4 have not been reported before. Do these three seeding-specific polymorphs represent the presently unknown conformations of patient-extracted seeds, that is, of pathogenic hIAPP fibrils (Supplementary Text 4)?

A warning that seeded structures do not always replicate structures of the seeds comes from the recent seeding study of Lövestam et al[33]. This work suggests that fibrils of recombinant α-synuclein seeded by patient extracts do not inevitably replicate the structures of the seeds[33]. In this α-synuclein study, two parallel seeding attempts using different patient extracted seeds generated seeded fibrils whose structures were determined. The structures were composed of two types of protofilaments that are either essentially identical or close to that found in un-seeded recombinant α-synuclein fibrils. However, a third parallel

seeding attempt generated fibrils that largely replicate one out of two protofilaments of the seeds[33]. We believe these results suggest that a risk of seeding is that the seeded protein may form fibrils that adopt the un-seeded conformation even in the presence of seeds. The third attempt in Lövestam, et al. actually demonstrated that the structure of the seeds from the daughter fibrils can be obtained, at least at the level of the core fold of the protofilament. This emphasizes the importance of comparing the seeded fibril structures with un-seeded controls at the protofilament level to judge which protofilament may represent the conformation of the seeds.

When we investigate the three new polymorphs found only in seeded hIAPP fibrils (TW1, TW2, and TW4) at the protofilament level, we find TW2 adopts a unique conformation (CF3). Therefore, we think that CF3 is the most likely conformation to represent the seeds. In contrast, TW1 and TW4 both contain CF1 and CF2 which also exist in other un-seeded hIAPP fibrils. We think this finding does not diminish the possibility that the structure of TW1 and TW4 are inherited from pathogenic hIAPP fibrils. Our reason is that, although TW1 and TW4 both contain a protofilament with CF1 that has been observed in the un-seeded controls 6Y1A[15] and 6ZRF[16], TW1 and TW4 differ from these un-seeded controls in that they also contain a protofilament with CF2. Therefore, the protofilaments that adopt CF2 can be considered as structural elements derived from the pathogenic seeds. We note that CF2 is also found in other un-seeded hIAPP fibrils when either S20G (in 6ZRR and 6ZRQ[16]) or SUMO-tagged (in 6VW2[12]) hIAPP was used as starting monomer. Therefore, we believe that CF2 can be adopted either through seeding with pathogenic fibrils or through changing the form of hIAPP used for un-seeded fibril growth.

Additional factors may mitigate concern about the seeding fidelity in the present study. First, Lövestam et al suggest that their failure to replicate structures via seeding may be due to the truncation and post-translational modification (PTM) of pathogenic α-synuclein fibrils[33]. These PTMs include ubiquitination and phosphorylation and are considered to favor α-synuclein fibril formation in patients as does C-terminal truncation[34,35]. Apparently when recombinant α-synuclein without PTMs or truncation was used for seeding, the daughter fibrils do not adopt the same structure as the seeds. However, PTMs other than the C-terminal amidation, which is present in our hIAPP monomer, or truncation are not required for hIAPP amyloidosis[36]. Furthermore, in contrast to previously determined, un-seeded hIAPP fibril structures that mostly contain the C-terminal portion of hIAPP in the fibril core with the first visible residue around 13–15 (Extended Data Fig. 5A), residues 6–12 are visible in TW2 and chain A of TW4, and adopt similar conformations in both structures (Extended Data Fig. 5B, insert). The conformation of residue 1–5 is also indicated by weak densities in TW2 and chain A of TW4 (Extended Data Fig. 5B). The observation of the longer cores in TW2 and TW4 may also support their potential pathological origin, because in vivo fibril formation is much slower that in vitro, which will give the N-terminus enough time to occupy a definite conformation. This hypothesis is further supported by the observation that α-synuclein fibrils extracted from patients' brains have larger ordered fibril cores than fibrils formed in vitro[18]. In short, the lack of sequence modifications, and larger ordered fibril cores may both suggest better fidelity of seeded replication of hIAPP structure. In addition, hIAPP amyloid is linked with β cell damage in T2D[37,38], and the observation

that our seeded hIAPP fibrils are toxic to pancreas cells (Extended Data Fig. 9B) may add to the potential physiological relevance of this study.

We note that if our structures indeed replicate the conformations of pathogenic hIAPP fibrils, these fibrils are extracted from only one T2D patient. Although fibrils formed by the same protein and formed in different patients with the same disease were shown to adopt same structures in tau and α-synuclein studies[18,39–41], it is still unknown if this is so for hIAPP fibrils in T2D. Further study with multiple patient samples is needed to address this question.

The origin of heterotypic pairings of hIAPP conformations

A notable finding in this study is that TW1 and TW4 are both composed of two protofilaments that adopt completely different conformations (Fig. 2, Fig. 3B, Extended Data Fig. 4A and Supplementary Text 5). Amyloid fibril structures with two protofilaments of different conformation have been reported several times (e.g. recombinant H50Q α-synuclein fibrils[42] and brain extracted α-synuclein fibrils[18]), but the difference in conformation between protofilaments has never been as large as we observe in TW1 and TW4 in this study and 6ZRR from synthetic S20G hIAPP[16]. We think these unique fibrils combining different conformations are the result of hIAPP's propensity to adopt different core folds, and the ability of these different conformations to interface via different surfaces (Extended Data Fig. 5F).

Conclusion

In summary, in this study we seeded fibril formation of synthetic hIAPP monomers with fibrils extracted from islet cells of a T2D patient and determined four cryo-EM structures of the seeded fibrils. Analysis of these structures and comparison with previously reported hIAPP fibril structures suggest the structural elements (CF3 and heterotypic assembly of CF1 and CF2) that are related to pathogenic hIAPP fibrils. The comparisons of wild-type to S20G hIAPP fibril structures and of hIAPP to Aβ fibril structures reveal the possible mechanism of how the hereditary mutation S20G facilitates hIAPP fibrilization in T2D and the regions that may enable hIAPP and Aβ cross-seeding.

Methods

Islet cells from donors with T2D

Islet cells from 7 donors with T2D were provided by City of Hope as formalin-fixed paraffin-embedded slices to test the existence of amyloid deposits by Congo red staining. The basic information of each donors was listed in Supplementary Table 1. After Congo red staining, we selected the donor with the highest staining signal (Case 6) and frozen islet cells from this donor were further requested from City of Hope and used for genotyping and fibril extractions.

Congo red staining of fixed patient slices

Formalin-fixed paraffin-embedded slices of islet cells (5 μm thickness) were baked at 45 °C for 20 minutes for deparaffinization. After that, the slices were soaked in Xylene (Fisher

Scientific) for 5 minutes for 3 times, and then washed by 100%, 95%, 70%, and 50% of ethanol for 4 minutes, 4 minutes, 2 minutes and 2 minutes, respectively. The washed slices were soaked in water for 10 minutes on a shaker. The slices were Congo red stained by Amyloid Stain, Congo Red Kit (Sigma-Aldrich) following the instruction of the kit. After Congo red staining, the slices were dipped twice in Hematoxylin (Thermo Scientific) and rinsed by water for counter staining. After staining, the slices were washed with 100% ethanol for 5 minutes for 3 times, rinsed by Xylene, mounted with Permount Mounting Media (Fisher Scientific), and let dry for several hours. Stained slices were imaged by AXIO Observer D1 Fluorescence Microscope (Zeiss) using bright field and polarized light.

Genotyping of Case 6 hIAPP

To identify the genotype of hIAPP from Case 6, we extracted genome DNA from the islet cells using the following protocol: frozen islet cells were re-suspended with 400 μl of SNET buffer (20 mM Tris pH 8.0, 5 mM EDTA, 1% SDS, 400 mM NaCl) supplemented with 0.5 mg/ml Protease K, and the solution was incubated at 50 °C with occasional shaking for 1 hour. After incubation, the solution was mixed with 400 μl Phenol Chloroform, vortexed for 15 seconds, and centrifuged at 14,000 × g for 30 seconds. The top aqueous layer of the mixed solution was removed and mixed with 40 μl 3M Sodium Acetate pH 5.4, 0.5 μl GlycoBlue (Thermo Scientific), and 750 μl isopropanol. The mixed solution was incubated at −20 °C for 20 minutes, and then centrifuged at 14,000 × g for 30 seconds. The supernatant was then removed, and the pellet was washed with 400 μl ethanol and further centrifuged at 14,000 × g for 30 seconds. The supernatant was discarded and the tube was air dried at room temperature for 20 minutes. Finally, 50 μl distilled water was added into the tube to dissolve the pellet, and the solution was used as template for PCR using in-house designed primers to amplify the DNA fragments that contain hIAPP gDNA. The PCR products were sequenced by Laragen (USA).

The sequencing experiments were done independently three times using three independent PCR products, and all results show the genotype of hIAPP from Case 6 is the wild type. One of the representative sequencing result is shown as follows, in which the sequence of a part of the genome DNA that contains hIAPP gDNA is shown. The sequences of the in-house designed primers are underlined, the sequence of hIAPP (residues 1–37) gDNA is shown in bold, the DNA fragment that have unambiguous sequencing result is shown in gray background, and the codon of Ser20 is boxed.

…
AAAAAAAAATCTCAGCCATCTAGGTGTTTGCAAACCAAAACACTGAGTTACTTAT
GTGAAAATTGTTTCTTTGGTTTTCATCAATACAAGATATTTGATGTCACATGGCTGG
ATCCAGCTAAAATTCTAAGGCTCTAACTTTTCACATTTGTTCCATGTTACCAGTCAT
CAGGTGGAAAAGCGG**AAATGCAACACTGCCACATGTGCAACGCAGCGCCTGG**
CAAATTTTTTAGTTCATTCCAGCAACAACTTTGGTGCCATTCTCTCATCTACC
AACGTGGGATCCAATACATATGGCAAGAGGAATGCAGTAGAGGTTTTAAAGAGA
GAGCCACTGAATTACTTGCCCCTTTAGAGGACAAT...

Fibrils extraction from islet cells and immunoprecipitation

The fibril extraction was performed according to a previous protocol[43]. Frozen islet cells were re-suspended with 700 μl of saline buffer (0.15 M NaCl), homogenized and centrifuged at 19,000 × g at 4 °C for 20 minutes. The supernatant was removed (referred to as S1 fraction) and the pellet was re-suspended with 400 μl saline buffer, homogenized and centrifuged as previous step. The supernatant was also removed (referred to as S2 fraction) and this 400 μl saline wash step was repeated for another 5 times (generating S3-S7 fractions). After that, the pellet was further washed with 400 μl H_2O with the same operation for 3 times (generated S8-S10 fractions). The final pellet was lyophilized and then re-dissolved with 100 μl TBS buffer (20 mM Tris, pH 7.6, 150 mM NaCl) and was referred to as the pellet (P). Here we found hIAPP fibrils are enriched mainly in the S1 fraction but not in the pellet as described previously[43], by dot-blot assays and negative stain EM (Extended Data Fig. 1B&C). We think this discrepancy is a consequence of the different tissues used for fibril extraction. In the previous study, frozen pancreatic tissues were used[43], whereas we used purified islet cells instead. In our case, the fibrils may be isolated much more easily, remaining in the supernatant of the first homogenization step. To assess the purity of the S1 fraction, we performed SDS-PAGE and ran a Western blot, probing with antibodies that target hIAPP, Aβ, tau, or α-synuclein (Extended Data Fig. 9A). The results suggested that only hIAPP fibrils were present in the S1 fraction, enabling further purification of S1 fraction via immunoprecipitation with fibril-binding OC antibody.

Before immunoprecipitation, we treated S1 fraction with Collagenase by mixing 60 μl of S1 fraction with 60 μl TBS buffer supplemented with 4 μM of $CaCl_2$ and 50 U/ml Collagenase (Sigma), and we incubated the mixed solution for 1 hour at 37 °C. To pull-down amyloid fibrils, we first coupled the antibody coupled magnetic beads by incubating 2 μg of Anti-amyloid fibrils OC antibody (Millipore, Lot no. 2345063) with 50 μl of protein A magnetic beads (Invitrogen) and diluted into TBST buffer (20 mM Tris, pH 7.6, 150 mM NaCl, 0.1% Tween 20) with 700 μl of final volume, and the mixed solution was incubated on a tube rotator at room temperature for 1 hour. After incubation, we collected the magnetic beads, discarded the supernatant, mixed the beads with 120 μl of Collagenase treated S1 fraction, and diluted the solution to final volume of 200 μl with TBS buffer. The final solution was incubated on a tube rotator at room temperature for 2 hours, and the beads were then collected (the supernatant was removed and referred to as flow through fraction). Collected beads were first eluted with 150 μl TBST buffer (elute-1 fraction), and then eluted twice with 50 μl of 100 mM glycine, pH 2.0, and neutralized with 1M Tris-HCl, pH 9.0 (elute-2 and -3 fraction). The eluted beads were re-suspended with 50 μl TBS and referred to as beads fraction. Here we found the hIAPP fibrils were enriched in elute-1 fraction, as judged by three criteria: (1) the observation of amyloid fibrils in electron micrographs, (2) the competence of elute-1 fraction in seeding the aggregation of fresh hIAPP monomers, and (3) positive anti-hIAPP and OC signals in dot-blots compared to the absence of primary antibody (Fig. 1B&C, Extended Data Fig. 1D–F, Supplementary Text 6).

We note that the existence of hIAPP fibrils in elute-2 fraction cannot be fully ruled-out by dot-blot, as elute-2 already contained significant amount of OC antibody (as shown in “no primary” line in Extended Data Fig. 1D as a negative control) so that the signal may be

saturated, whereas in EM and seeding assays the elute fractions did not suggest the presence of hIAPP fibrils compared to the elute-1 fraction (Extended Data Fig. 1D–F). We think the reason that hIAPP fibrils were not enriched in the elute-2 or -3 fractions is that the binding between hIAPP fibrils and OC antibody is not very strong, so that after the hIAPP fibrils were pulled-down from the solution they can be easily separated from the antibody when a slight buffer change occurred during the elute-1 step (from half diluted TBS to TBST, see above for detail), before a larger buffer change occurred at the elute-2 or -3 step.

Dot blot and Western blot

In our dot blot assay, 2 μl of each sample solution was pipetted onto multiple nitrocellulose membranes (Invitrogen) in parallel and allowed to dry for 15 minutes. The membranes were probed by Amylin Polyclonal Antibody (also referred as anti-hIAPP antibody in this study, Invitrogen, Lot no. UH2833361, 1:1000 dilution) or Anti-amyloid fibrils OC antibody (Millipore, Lot no. 2345063, 1:5000 dilution) respectively, and further probed by Anti-Rabbit IgG (Sigma, Lot no. 023M4757, 1:5000 dilution) as the secondary antibody, and visualized with ECL Plus Western blotting Substrate kit (Thermo Scientific). For an explanation for the high intensity in the “no background” dot blot of elute-2 (Extended Data Fig. 1D), see previous section.

In Extended Data Fig. 9A, we used Western blot to analyze the molecular weight of the S1 fraction. The loading dye contained 2M urea. Proteins were transferred to nitrocellulose membranes (Invitrogen) and detected by immunoblot analysis with Amylin Polyclonal Antibody (Invitrogen, Lot no. UH2833361, 1:1000 dilution), anti-tau antibody (Agilent Dako, Lot no. 20024929, 1:5000 dilution), anti-Aβ antibody 6E10 (Biolegend, Lot no. B261546, 1:5000 dilution), and anti-α-synuclein antibody (MJFR-14-6-4-2, Abcam, Lot no. GR3222269-10, 1:5000 dilution). As a secondary antibody, we used goat anti-rabbit HRP (Invitrogen, Lot no. 2116291, 1:5000 dilution) or goat anti-mouse HRP (Abcam, Lot no. GR3271082-2, 1:5000 dilution). All membranes were developed using Pierce™ ECL Plus substrate (Thermo Scientific). We used positive controls to validate the antibodies for Aβ1–42 (expected size ~4 kDa, for anti-Aβ antibody), tau-K18 (residues 244–372, expected size ~15 kDa, for anti-tau antibody), and α-synuclein 1–140 (expected size ~14 kDa, for anti-α-synuclein antibody).

Negative stain transmission electron microscopy

Negative-stain transmission EM samples were prepared by applying 5 μl of solution to 400 mesh carbon-coated formvar support films mounted on cooper grids (Ted Pella, Inc.). The grids were glow-discharged for 30 seconds before applying the samples. The samples were incubated on the grid for 2 minutes and then blotted off with a filter paper. The grids were stained with 3 μl of 2% uranyl acetate for 1 minute and washed with an additional 3 μl of 2% uranyl acetate and allowed to dry for 1 minute. The grids were imaged using a T12 (FEI) election microscope.

Synthetic hIAPP preparation

Synthetic full-length hIAPP peptide was ordered from InnoPep (San Diego, USA) with an amidated C-terminus and a disulfide bond between Cys2 and Cys7, and the purity is

>95%. The peptide was dissolved in 100% 1,1,1,3,3,3-hexafluoro-2-propanol (HFIP) at a concentration of 1 mM, sonicated at 4 °C for 1 minute, and incubated at room temperature for 5 hours. After incubation, HFIP was evaporated by a CentriVap Concentrator (Labconco) and the peptide was then stored at −20 °C. Before use, HFIP treated peptide was dissolved in 100% DMSO at a concentration of 1 mM or 5 mM, and further diluted 100-fold in PBS and filtered with 0.1 μm Ultrafree-MC-VV centrifugal filters (Millipore) to form 10 μM and 50 μM hIAPP solutions.

ThT seeding assays

Synthetic hIAPP was diluted to 10 μM or 50 μM in PBS supplemented with 30 μM ThT, filtered with 0.1 μm Ultrafree-MC-VV centrifugal filters (Millipore), and mixed with 1% or 5% (v/v) of seeds, respectively. The seeds were sonicated at 4 °C for 3 minutes before use. Mixed solution was pipetted into a polybase black 384-well plate with optical bottom (Thermo Scientific) and incubated at 37 °C without shaking. ThT fluorescence was monitored by FLUOstar Omega plate reader (BMG LABTECH) with excitation and emission wavelengths of 440 nm and 480 nm, respectively. The fluorescence curves were averaged from three independent measured replicates and error bars show s.d. of replicate readings. To normalize the different ranges of fluorescence readings observed from different experiments (probably due to the different fluorescence gain settings of the plate reader), we normalized the readings to make the minimum mean value in each panel 0% and the maximum mean value in each panel 100%. To test the seeding ability of different fractions from the immunoprecipitation assay, 10 μM hIAPP solution was mixed with 1% (v/v) of these fractions (elute-1, -2 and -3) as fibril growing seeds (results shown in Extended Data Fig. 1F). To monitor the seeding effect at the same concentration as growing fibrils for cryo-EM structure determination, 50 μM hIAPP solution was mixed with or without 5% (v/v) the elute-1 fraction from immunoprecipitation as patient extract (shown in Fig. 1C). ThT curves were generated using GraphPad Prism.

Fibril growth and seeding

To obtain high fibril yields necessary for cryo-EM studies, we raised the concentration of hIAPP monomers from 10 μM used in seeding assays shown in Extended Data Fig. 1F to 50 μM. We were concerned that the elevated concentration of hIAPP would enhance the growth of unseeded amyloid fibrils and divert monomer from being templated by seed. However, we found that seeding at this elevated hIAPP concentration still had a strong effect; it significantly increased the aggregation rate and ThT signal compared to the monomers incubated in the absence of seeds (Fig. 1C). Imaging samples prepared by 20 hours of incubation, we found the monomers incubated with seeds show mature and elongated fibrils whereas the monomers incubated alone show immature fibrils (Fig. 1D). This observation further suggested the efficacy of seeding.

Freshly diluted and filtered 50 μM hIAPP solution in PBS was mixed with 5% (v/v) patient extract as seeds. The seeds were sonicated at 4 °C for 3 minutes before use. The solution was then incubated at 37 °C without shaking for 20 hrs. After incubation, the solution was centrifuged at 4,000 × g for 1 minute, and 95% of the original volume of supernatant was carefully removed from the centrifuge tube to concentrate the fibril solution 20 times.

The remaining fibrils were resuspended by mixing with a pipet and used for cryo-EM data collection. We tested the cytotoxicity of the seeded fibrils used in cryo-EM by MTT assays (Extended Data Fig. 9B).

Cryo-EM data collection and processing

To prepare the grids for cryo-EM data collection, we applied 2.6 μl of fibril solution onto a Quantifoil 1.2/1.3 electron microscope grid which was glow-discharged for 2 minutes before use. The grid was plunge frozen into liquid ethane with a Vitrobot Mark IV (FEI). Two datasets were collected on the same 300 kV Titan Krios (FEI) microscope with a Gatan K3 camera located at the HHMI Janelia Research Campus, and were collected from grids that were made in parallel from the same batch of fibril samples. The microscope was operated with 300 kV acceleration voltage and slit width of 20 eV. Movies were collected using super-resolution mode with a nominal physical pixel size of 1.065 Å per pixel (0.5325 Å per pixel in super-resolution movie frames) with a dose per frame of ~1.5 $e^{-}/Å^2$. Fifty seven frames were taken for each movie for the first dataset (total dose per image ~85.5 $e^{-}/Å^2$) and 30 frames were taken for each movie for the second datasets (total dose per image ~45 $e^{-}/Å^2$). Automated data collection was driven by SerialEM[44]. Anisotropic magnification distortion estimation, CTF estimation and beam-induced motion correction were performed with mag-distortion-estimate[45], CTFFIND 4.1.8[46] and Unblur[47], respectively. The physical pixel size was corrected to 1.055 Å/pixel after anisotropic magnification correction with Unblur[47].

Particle picking was performed manually using EMAN2 *e2helixboxer.py*[48] for the first dataset, and performed automatically using CrYOLO[49] for the second dataset. Particle extraction, two-dimensional classification, helical reconstruction, and 3D refinement were performed in RELION[50,51]. Particles were extracted using an inter-box distance of 14.1 Å and a box size of 768 pixels that down-scaled to a box size of 384 pixels (bin factor equals to 2). We performed 2D classification with tau_fudge factor set to 2, and from 2D classes we were able to identify four morphologies with twisting features and another four morphologies without twisting features (named TW1-4 and NT1-4, respectively, see Fig. 2 and Extended Data Fig. 2). The disruption of each morphology was shown in Fig. 2 insert. We were only able to pursue the morphologies with twisting features due to the limitation of helical reconstruction. We selected the particles that belonged to 2D classes of TW1-4, and re-extracted them (individually for each morphology) into box size of 256 pixels (for TW1, TW3, and TW4, which have relatively short pitch), or box size of 384 pixels (for TW2, which has relatively long pitch). No down-scaling was used for re-extraction, and inter-box distance was kept to 14.1 Å. The helical parameters of each twister morphology were estimated from the measured crossover distance and used for further 3D classification. We performed 3D classification with K=3 (or K=5 for TW2) and a Gaussian cylinder initial model as described previously[12]. Particles belongs to the best 3D class were selected and several more rounds of 3D classification (K=3) were performed for each TW morphology to make sure the best particles were selected. The tau_fudge factor was set to 4 in the beginning of each 3D job, and was increased up to 64 to push the resolution of the reconstructions. We then use the particles selected from the 3D classification to perform high-resolution gold-standard refinement[51], and the resolution of

each reconstruction was estimated using the 0.143 Fourier shell correlation (FSC) resolution cutoff. Before performing gold-standard refinement of TW2, we re-extract the selected particles from 384 pixel box size to 256 pixel box size in order to get higher quality final map.

Previous structural studies of unseeded synthetic wild-type hIAPP fibrils both show structures that are similar to TW3 (PDB 6Y1A[15] and 6ZRF[16], Extended Data Fig. 4B), whereas there two structures were reconstructed with different handedness (right-handed twist for 6Y1A[15] and left-handed twist for 6ZRF[16], respectively). Because in this study we were not able to achieve resolutions high enough to identify the handedness of each morphology, here we performed reconstructions by assuming all TW morphologies are left-handed, as the left-handed twist are most common for amyloid fibrils. We note that we cannot rule out the possibility that one or serval of the TW morphologies solved here are right-handed. We believe the handedness should not influence the model we built for each morphology, as in the current resolution the same fold can be generated with either handedness, which is supported by the observation that 6Y1A and 6ZRF adopt similar structure but have different handedness. Therefore, we believe determining the handedness should be beyond the scope of this study, as we mostly focus on the structures within each layer of the fibrils here.

Atomic model building

The refined maps were sharpened via phenix.auto_sharpen[52] at the resolution cutoff indicated by half-map FSC. The atomic model of each TW morphology was manually built into the sharpened map using COOT[53]. For TW1, the map clearly suggests that a single layer contains two asymmetric chains. To build each chain, we first located the C-terminal tyrosine residue (Tyr37) at the end of the density tube that does not have extra fuzzy density. The remaining residues were built de novo according to their position in sequence relative to Tyr37. The resulting model fits the map unambiguously for all side chains (except a bump in TW1, see Supplementary Text 7).

The initial models were extended to five layers (ten chains) based on the helical symmetry of each TW morphology, and the five-layer models were refined by phenix.real_space_refine[54] for several rounds. As the last step, the rotamer of each serine, glutamine and asparagine residue was manually inspected to favor the hydrogen binding, and the final model was validated using MolProbity[55].

Structural alignment of all reported hIAPP fibril structures

With the four structures reported in this study, there are currently nine near-atomic resolution structures of hIAPP fibrils (Table 2). To reduce the amount of structures used for comparison, we first used TW3 to represent 6Y1A[15] and 6ZRF[16] because these three structures are very similar to each other (Extended Data Fig. 4B). Meanwhile two morphologies from hIAPP S20G fibrils have almost identical conformation of chain A and B (6ZRR and 6ZRQ[16], and 6ZRR has an additional chain C in each layer), so we used 6ZRR to represent 6ZRQ. Here we performed structural alignment of these structures at the single chain level. That is, for those structures that contain two identical monomers in

each layer (i.e. TW3), only chain A was used for structural alignment; for structures that contain two monomers with different structures (i.e. TW1), both chain A and B were used for structural alignment; for 6ZRR that contain two identical monomers (chain A and B) and one additional monomer with different fold (chain C), chain A and C were used for structure alignment. The alignment was done via Pymol[56]. Initially all residues in each chain were used for structural alignment, and after all chains had been categorized into CF1 and CF2, all chains with CF1 fold were re-aligned with the residue range restricted to 15–28 and that with CF2 fold were re-aligned with the residue range restricted to 20–33.

We note that our previously reported SUMO-tagged recombinant hIAPP fibril structure contains CF2 when the swapped version was used for structural alignment. The swapped version of 6VW2 was proposed in our previous structure study of hIAPP fibrils[12], which is formed by swapping the residues from two chains in a single layer at Gly24 that are very close to each other (Extended Data Fig. 6, also see red dash line in Fig. 3B); this domain swap was predicted to be chemically and energetically plausible although not supported by the density map of 6VW2[12].

We note that in this study we only used cryo-EM structures of hIAPP for structural comparison and analysis, whereas there are models of hIAPP fibrils reported previously that were generated via different methods[13,14]. These alternative models, especially the one from the nuclear magnetic resonance (NMR) study, may represent the structure of the ribbon morphology of hIAPP fibrils which cannot be readily determined by cryo-EM. In our seeded fibrils, we also observed four morphologies of ribbon form of hIAPP fibrils (NT1-4, Extended Data Fig. 2A&B) which together composed 35% of total population and are not amenable for cryo-EM structure determination. We cannot rule out the possibility that the structures of NT1-4 may be similar to the NMR model.

Structural alignment of hIAPP and Aβ fibril structures

PDB IDs of Aβ structures used for structural alignment are: 6OIZ[57], 2M4J[58], 2MVX[59], 5KK3[60], 5OQV[61], 2NAO[62], 2MXU[63], 2BEG[64], 2LMN[65], 2MPZ[66], and 6SHS[67]. Structural alignment was done via Pymol[56]. We aligned each Aβ structure with TW1 chain A, chain B and TW2 using residues 24–34 in each Aβ structure and residues 19–29 in hIAPP fibril structures. The r.m.s.d. of each alignment is summarized in Supplementary Table 3.

MTT assays

Rin5F cells were purchased from ATCC (Cat. # CRL-2058). 90 μL of cells were plated at 60,000/ml cells, in 96-well plates (Cat. # 3603, Costar, Fisher Scientific) in DMEM media (Life Technologies, cat. 11965092) supplemented with 10% (vol/vol) FBS (Life Technologies, cat. A3160401), 1% penicillin/streptomycin (Life Technologies, cat. 15140122), and 1% Glutamax (Life Technologies, cat. 35050061) at 37 °C, 5% CO2 in a humidified incubator. To perform MTT assays, patient-fibril-seeded hIAPP fibrils in 50 μM of concentration were pelleted by centrifugation at 21,000 × g for 1 hour and supernatant was removed. The pellet was suspended in sterile PBS buffer and sonicated for 5 minutes, and 10 μL of sample solution was added to cells at various concentrations of 0, 1, 10 and 50 μM. Experiments were done in triplicate. After a 24-hour incubation of samples with

cells, 20 μL of Thiazolyl Blue Tetrazolium Bromide MTT dye (Sigma) was added to each well and incubated for 3.5 h at 37°C under sterile conditions. The MTT dye stock was prepared by dissolving 5 mg/mL in sterile PBS buffer. The MTT assay was stopped by carefully aspirating off the culture media and adding 100 μL of 100% DMSO to each well. Absorbance was measured at 570 nm and the background reading was recorded at 700 nm and subsequently subtracted from the 570 nm value.

Statistics and Reproducibility

The western blot, ThT, and cytotoxicity experiments were replicated at least three times with similar results. We did not replicate the Congo red staining. One negative stain EM grid was prepared and imaged for each sample, whereas multiple (more than three) micrographs with similar results were observed for each grid.

Extended Data

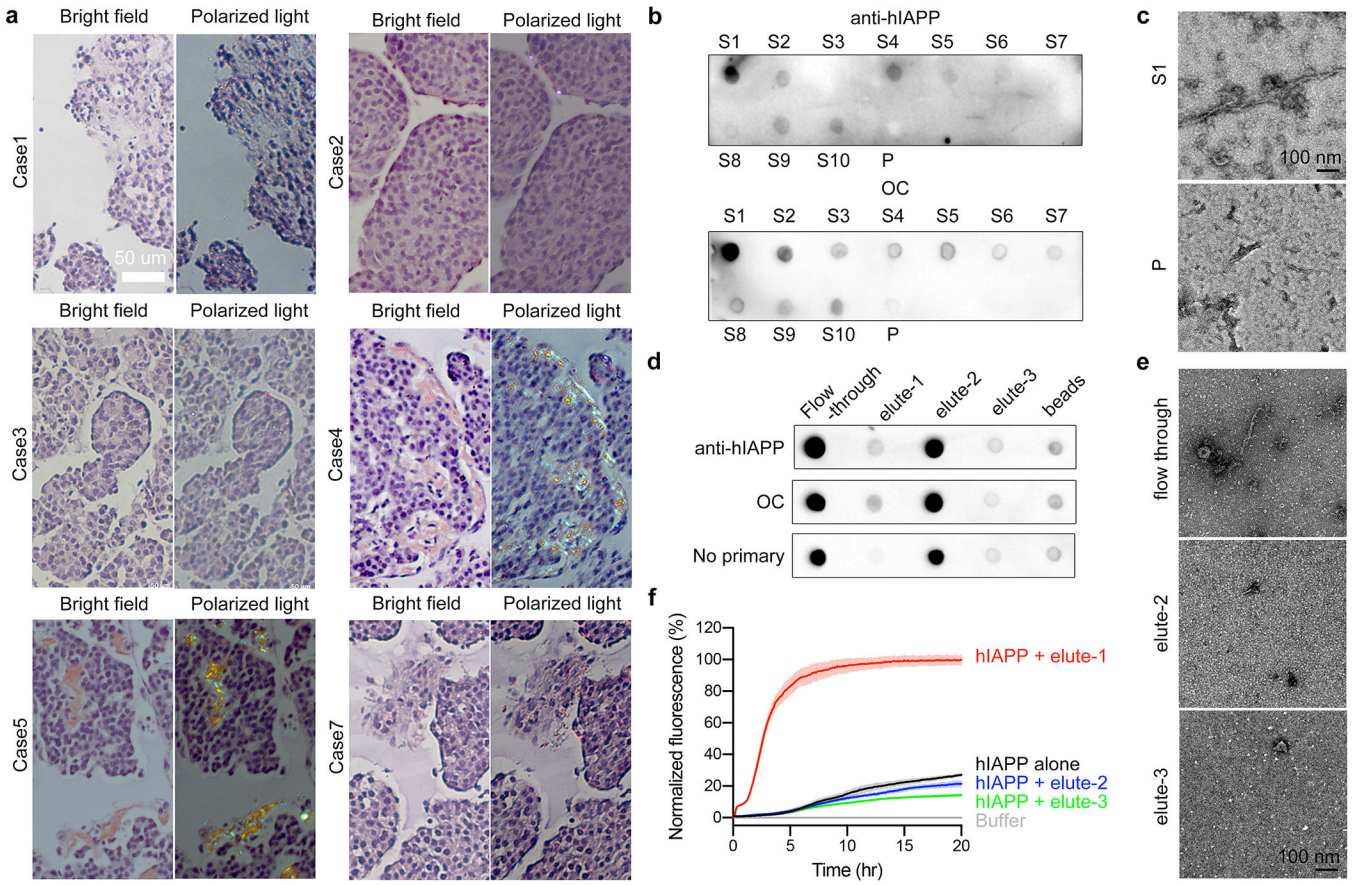

Extended Data Fig. 1. Supplemental information on extraction of patient islet cells and seeding of fibril growth.

a, Congo Red staining of slices of islet cells from various T2D donors (see Supplementary Table 1). b, Dot blot of fractions from extracted patient islet cells probed by anti-hIAPP (top) and anti-amyloid fibrils OC (bottom) antibodies. c, Negatively stained images of S1 and P fractions in (b). d, Dot blot of fractions from immunoprecipitation of the S1 fraction

probed by anti-hIAPP (top), OC (middle) antibodies and no primary antibody (bottom) as a base line. e, Negatively stained images of flow through, elute–2 and elute–3 fractions in (b). The EM image of the elute–1 fraction is shown in Fig. 1b. f, ThT aggregation curves of fresh prepared synthetic hIAPP peptide incubated alone (black) or with elute-1 (red), elute-2 (blue) or elute-3 (green) fraction in (d) as fibril growth seeds. Data are shown as mean ± s.d., n=3 independent experiments. Note the elute-1 fraction from immunoprecipitation shows notable seeding ability as its curve shows shortened lag time and stronger ThT readings compared to hIAPP alone, whereas the elute-2 and elute-3 fractions show no ability in altering the hIAPP aggregation curve. Please see Methods for the detailed definitions of fractions in panels b–f.

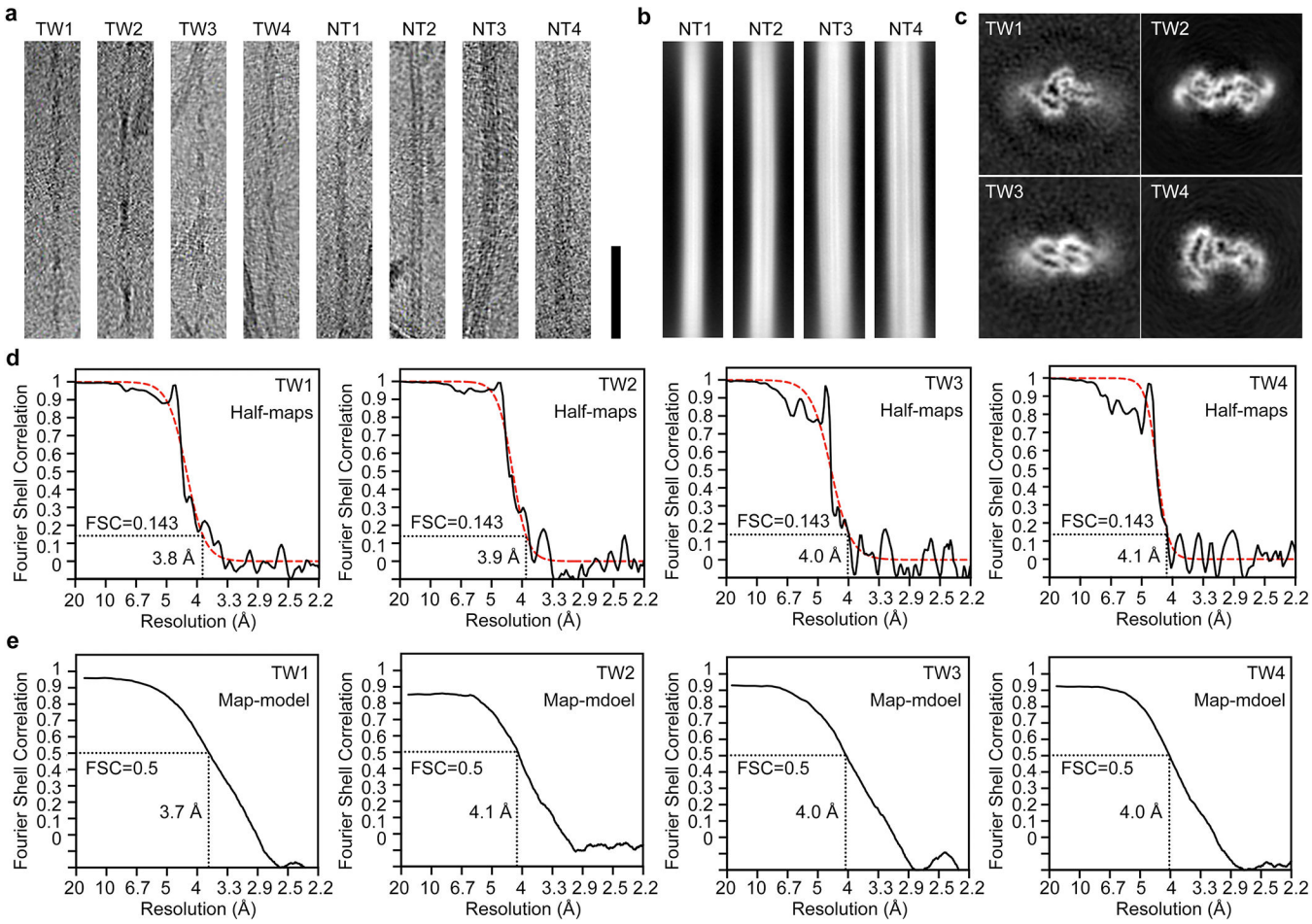

Extended Data Fig. 2. Cryo-EM data processing.

a, Representative micrographs of 8 identifiable morphologies during data processing (TW1-TW4 and NT1-NT4, scale bar 500 Å). b, Representative 2D classes of NT1-NT4. c, Central slices of final 3D reconstructions of TW1-TW4. d-e, FSC curves between two half-maps (e) and the cryo-EM reconstruction and refined atomic model (f). In half-maps FSC, FSC curves (black) are fitted (red) with the model function 1/(1+exp((x-A)/B)), with A=0.2328 and B=0.01517 for TW1, A=0.2347 and B=0.01234 for TW2, A=0.2255 and B=0.01427 for TW3, and A=0.2252 and B=0.009377 for TW4.

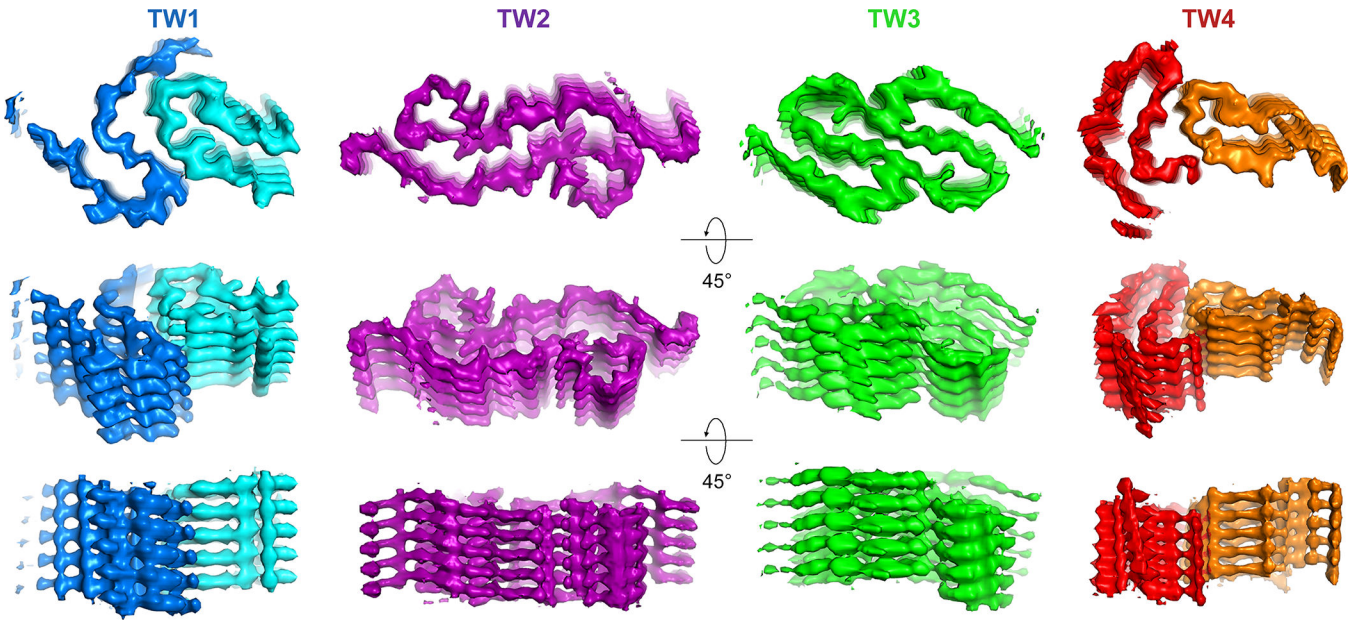

Extended Data Fig. 3. Different views of the cryo-EM maps with five layers shown.
For each morphology, the top view shows clear separation of β-strands, and the tilted views on the middle and bottom show clear separation of the layers of β-sheets along the fibril axis.

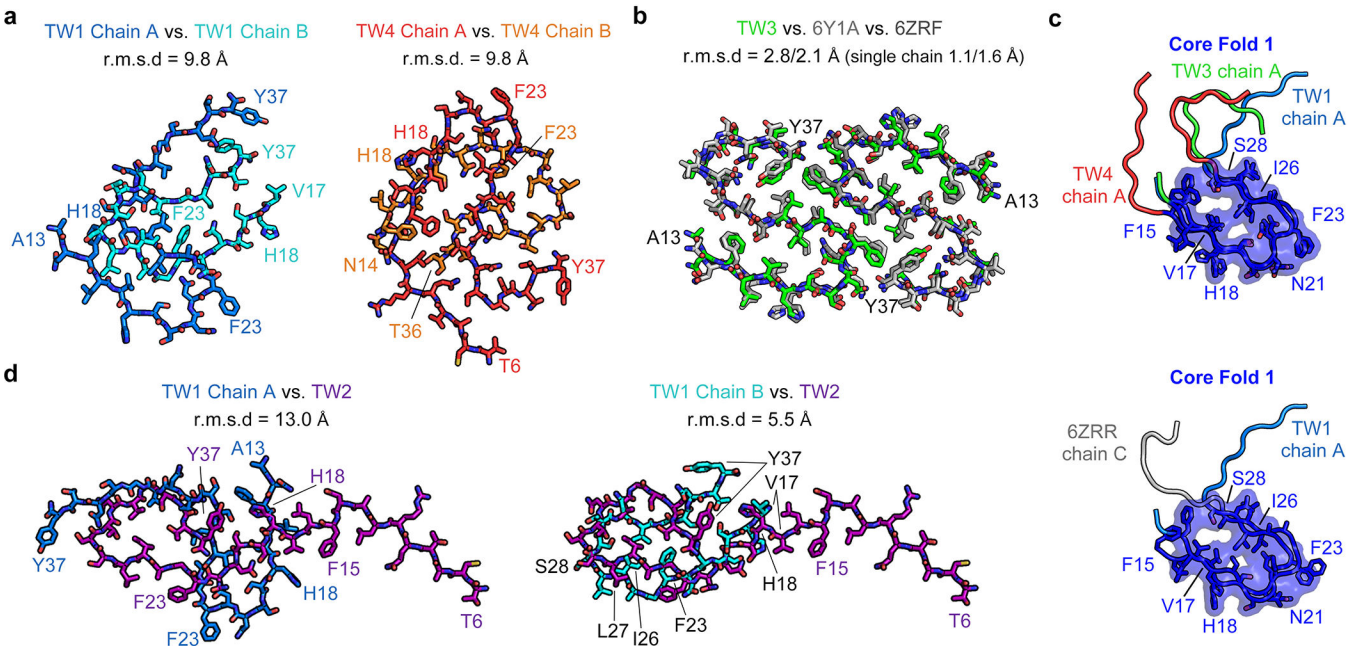

Extended Data Fig. 4. Structural comparisons of hIAPP fibrils.
a, Superposition of chain A and B of TW1 (left) and TW4 (right). b, Superposition of TW3, 6Y1A and 6ZRF, note that these three structures are very similar to each other. c, Superposition of chain A of TW1, TW3 and TW4 (top) and of TW1 chain A and 6ZRR chain C (bottom) at CF1 region. d, Superposition of TW1 chain A and TW2 (left), or TW1

chain B and TW2 (right). For superimposition details of panels a, b and d see Supplementary Table 2.

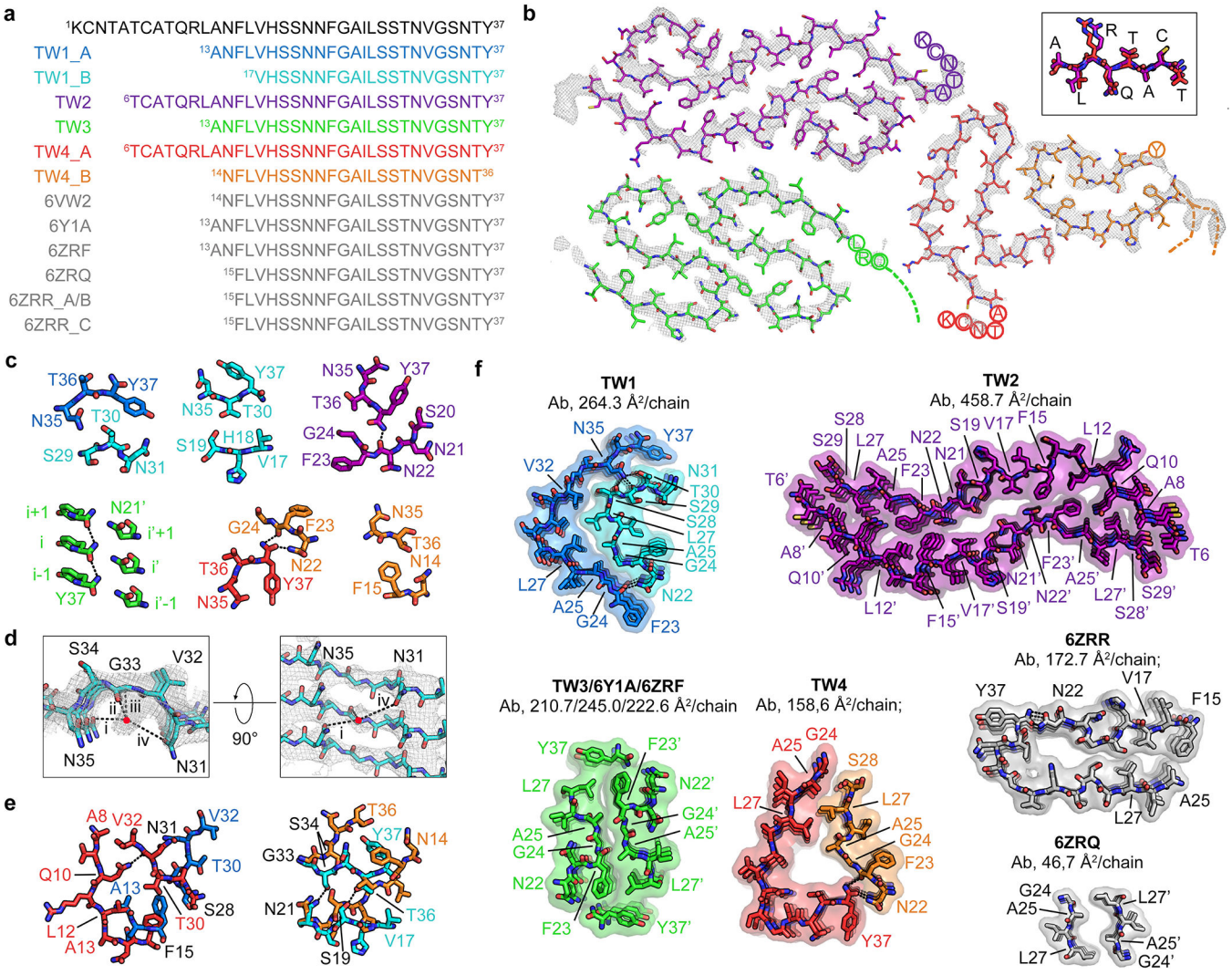

Extended Data Fig. 5. Detailed analysis of hIAPP fibril structures.

a, Above in black: the amino acid sequence of hIAPP; below: the residues visible in different hIAPP fibril structures. b, Plausible conformations of flexible N-termini of TW2 (purple), TW3 (green) and TW4 (red and orange) suggested by weak densities. The superposition of Thr6 to Ala13 region of TW2 and TW4 chain A is shown as an insert. c, The interactions around Tyr37 for TW1 (chain A, blue; chain B, cyan), TW2 (purple), TW3 (green), and TW4 (chain A, red; chain B, orange). d, The detailed view of an unexplained density around Gly33. The red dot represents the center of the unexplained density, and the length of each dash line is: i, 4.0 Å; ii, 2.9 Å; iii, 3.7 Å; iv, 5.2 Å. e, Different conformations of chain A of TW1 (marine) and TW4 (red, left) or chain B of TW1 (cyan) and TW4 (orange, right) outside the CF1 or CF2 region, respectively. TW1 and TW2 are superimposed at the CF1 (chain A) or CF2 (chain B) region. f, The interfaces between protofilaments A and B for TW1 (marine and cyan), TW2 (purple), TW3 (green), TW4 (red and orange), and 6ZRQ

(gray), as well as between protofilaments B (top) and C (bottom) for 6ZRR (grey). Ab, area buried. In panels c, e, and f, hydrogen bonds with distances between 2.3 and 3.2 Å are shown as black dashed lines. For superimposition details for panel b see Supplementary Table 2.

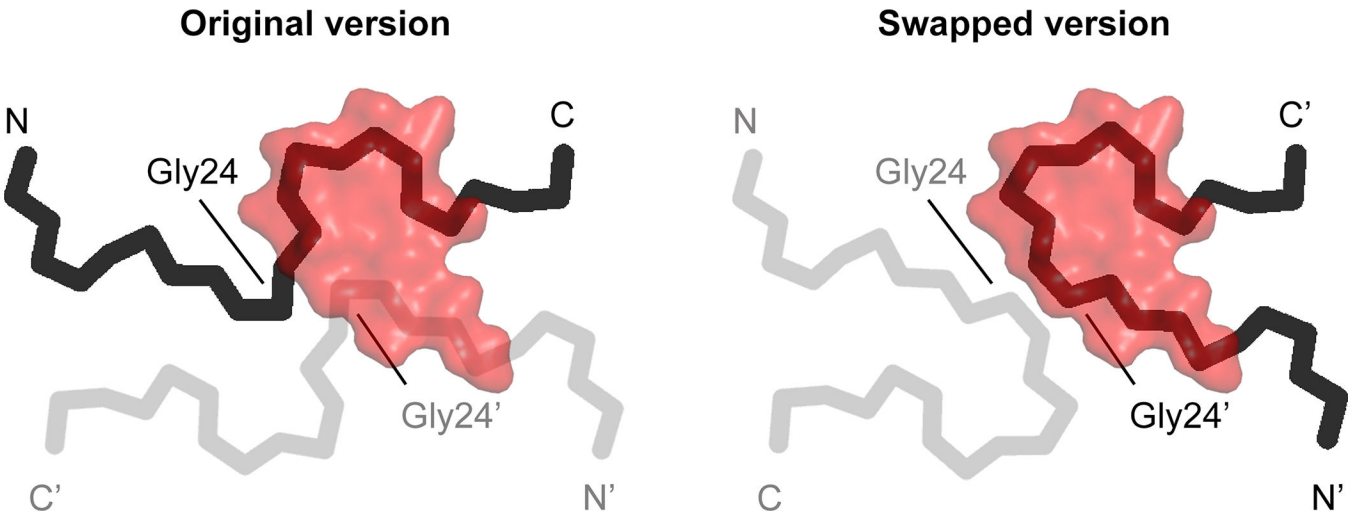

Extended Data Fig. 6. Explanation of swapped version of 6VW2.
Original version (left) and swapped version (right) of SUMO-tagged recombinant hIAPP fibril structure. Two symmetrically related chains are colored black and grey. CF2 was shown as surface and colored red.

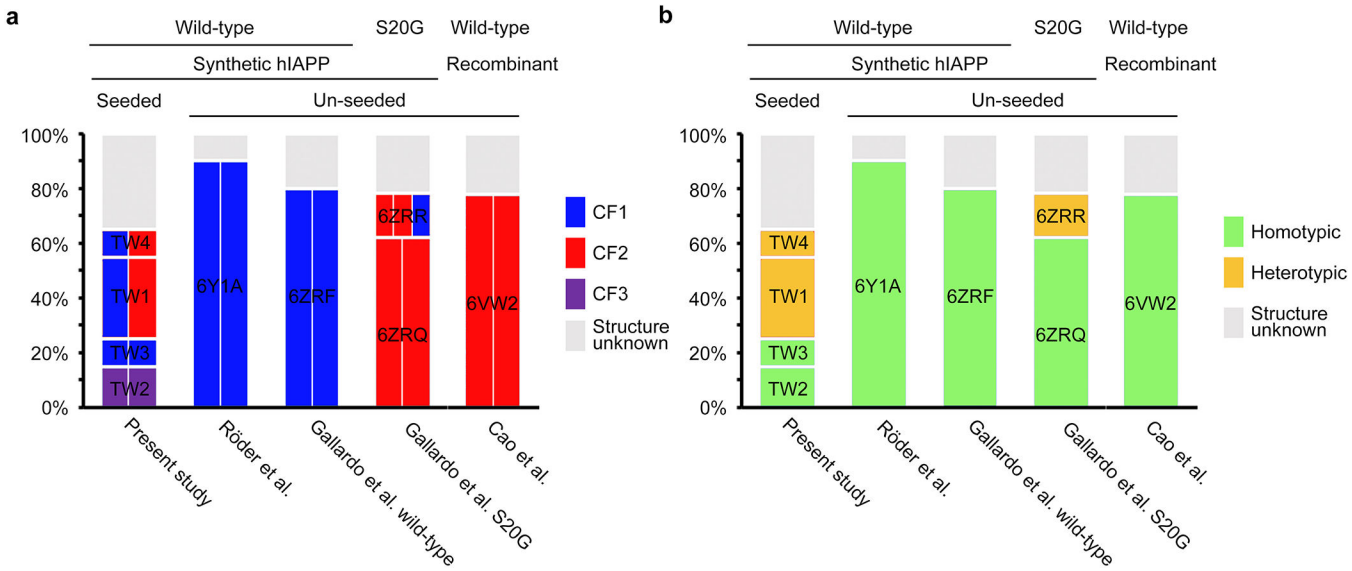

Extended Data Fig. 7. Distribution of different polymorphs in reported hIAPP cryo-EM datasets.
hIAPP polymorphs are colored by (a) core folds or (b) homotypic vs. heterotypic pairings. From panel a, we found CF2 is more abundant in S20G dataset compared to wild-type ones with the exception of 6VW2 dataset. In S20G dataset, 6ZRQ contributes to 76% of the solvable fibrils and is purely composed of protofilaments with CF2; 6ZRR contributes to the

other 24% and contains two protofilaments with CF2 and one protofilament with CF1. In contrast, wild-type fibrils, 6ZRF and 6Y1A are the only solvable species in their datasets and they contain only CF1 in their protofilaments; in the wild-type fibrils in this study, we also observe more protofilaments with CF1 than that with CF2. TW1 and TW4 have equal amount of protofilaments with CF1 and CF2, but TW3 contains only protofilaments with CF1. From panel b, we note when formed in vitro without patient seeds, we observed homo-dimer forms of fibrils in most datasets (Cao et al., Röder et al., and the wile-type of Gallardo et al.) and only in one dataset did we find a small portion of heterotypic species (S20G of Gallardo et al., in which 6ZRR contributes to 24% of the solvable population compared to 76% of 6ZRQ that is homo-dimer form). Whereas in patient-extract-seeded fibrils we see higher populations of heterotypic species (TW1 and TW4 contribute to 40% out of 65% of solvable population).

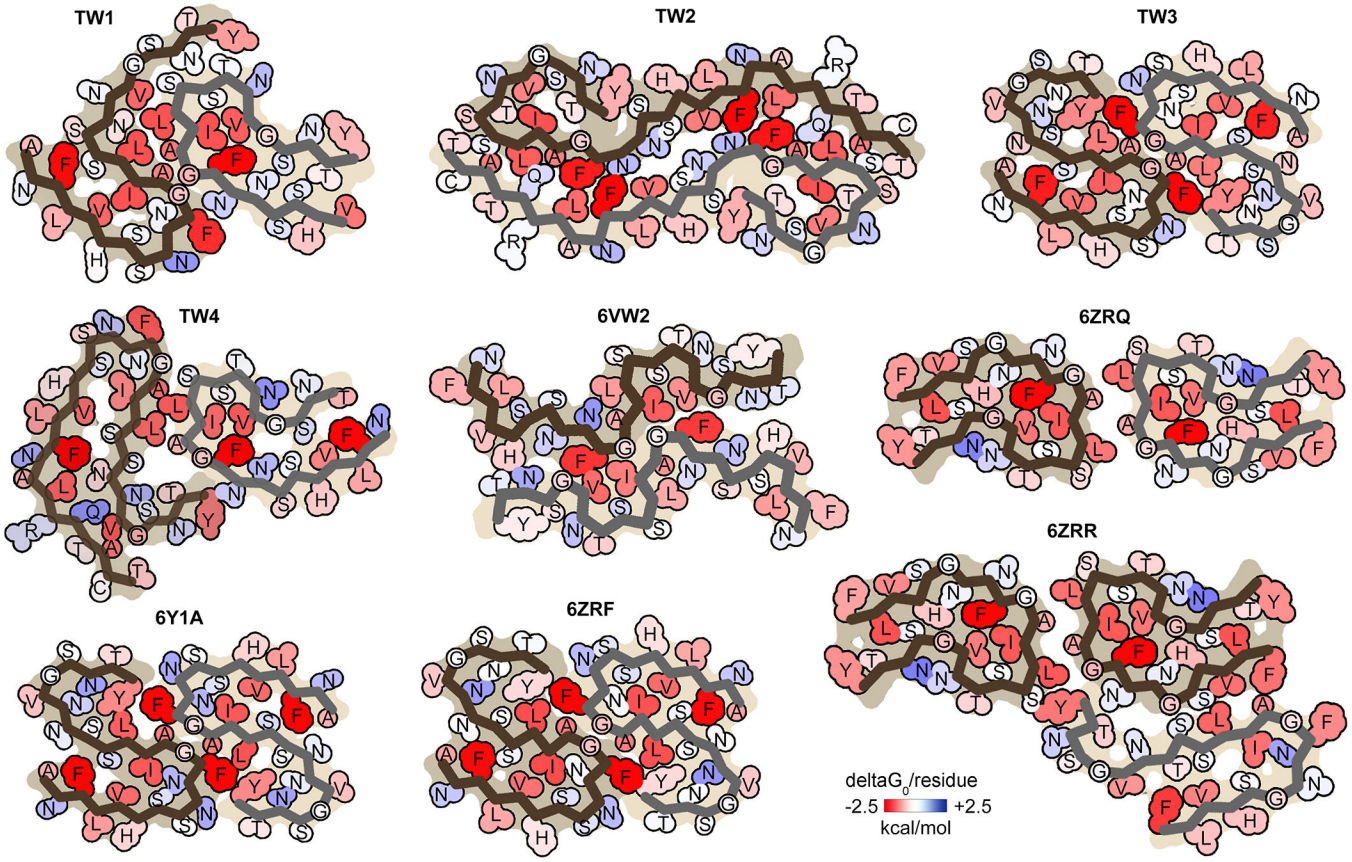

Extended Data Fig. 8. Solvation energy maps of reported cryo-EM hIAPP fibril structures.
Residues are colored from unfavorable (blue, 2.5 kcal/mol) to favorable stabilization energy (red, −2.5 kcal/mol).

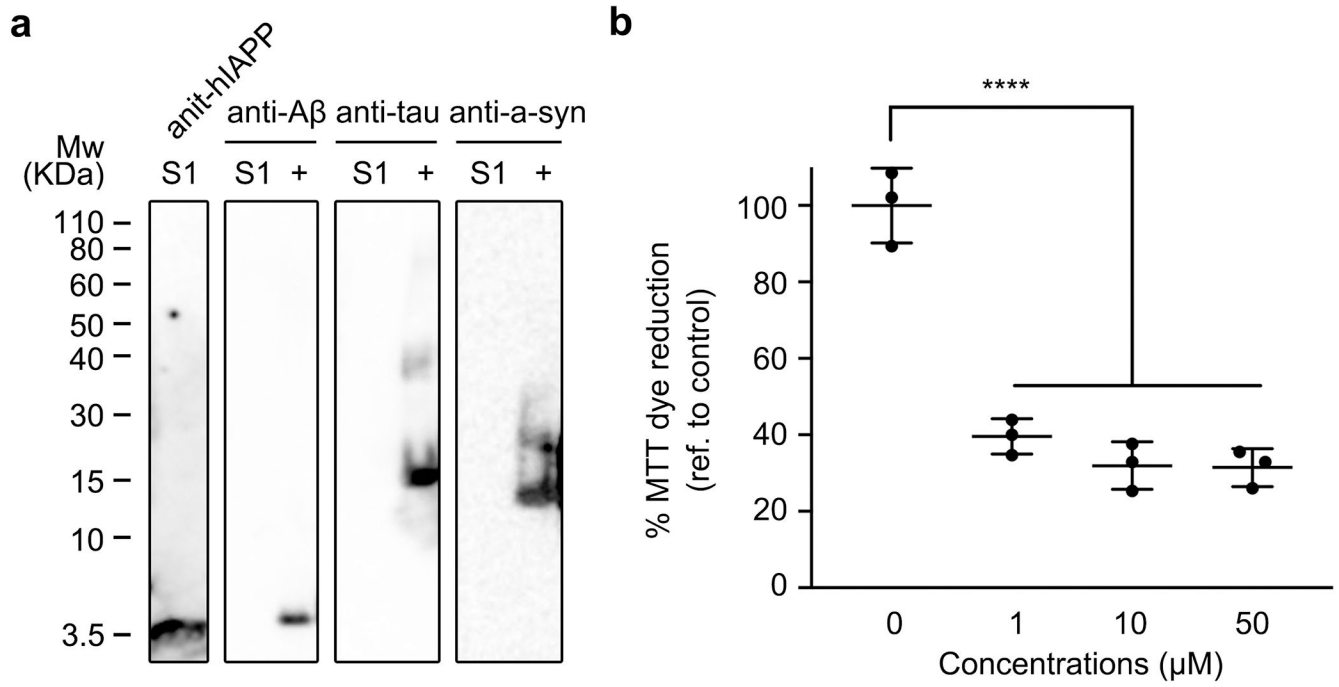

Extended Data Fig. 9. Western blot of S1 fraction of fibril extraction and MTT assays of seeded hIAPP fibrils.

a, Western blot of S1 fraction (originally characterized in Fig. S1b) probed by antibodies that target hIAPP, amyloid-β, tau (K18), and α-synuclein. The only antibody to recognize and label the S1 fraction is anti-hIAPP, suggesting that the S1 fraction consists primarily of hIAPP. Moreover, the molecular weight of the band corresponds to full-length hIAPP. When probed with amyloid-β, tau, and α-synuclein antibodies, bands appear only in positive control lanes (labeled as "+", see Methods for detail). b, Rin5F cells were treated with different concentrations of patient-fibril-seeded hIAPP fibrils, and significantly less MTT dye reduction was observed compared to cells without adding fibrils (****$p<0.0001$ using one-way ANOVA test, data are shown as mean ± s.d., n=3 independent experiments).

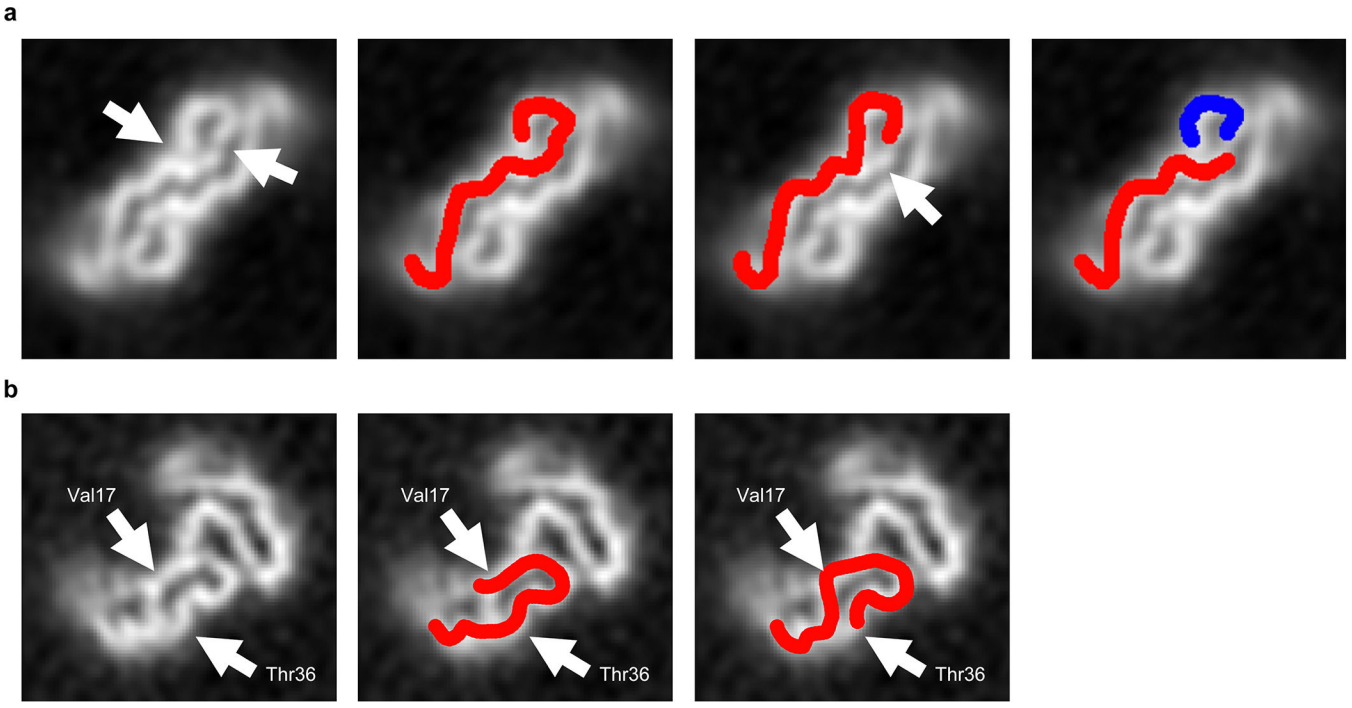

Extended Data Fig. 10. Main chain tracing of TW2 and TW4.
Low resolution 3D reconstructions of TW2 (a) and TW4 (b) displayed to illustrate the main chain tracing.

Supplementary Material

Refer to Web version on PubMed Central for supplementary material.

Acknowledgements:

We thank the Southern California Islet Cell Resources Center for providing human islets for this study. We thank X. Zhao at the HHMI Janelia Cryo-EM Facility for help in microscope operation and data collection. The authors acknowledge NIH AG 054022, NIH AG061847, and DOE DE-FC02-02ER63421 for support. D.R.B. was supported by the National Science Foundation Graduate Research Fellowship Program.

Data availability:

Structural data have been deposited into the Worldwide Protein Data Bank (wwPDB) and the Electron Microscopy Data Bank (EMDB) with accession codes: PDB 7M61, EMD-23686 (TW1); PDB 7M62, EMD-23687 (TW2); PDB 7M64, EMD-23688 (TW3); PDB 7M65, EMD-23689 (TW4). PDB accession codes for previously reported coordinates used for structural analysis in this study are: 6Y1A, 6ZRR, 6ZRQ, 6ZRF, 6VW2 for hIAPP fibrils and 6OIZ, 2M4J, 2MVX, 5KK3, 5OQV, 2NAO, 2MXU, 2BEG, 2LMN, 2MPZ, 6SHS for Aβ fibrils. All data is available in the manuscript or the supplementary materials.

References:

1. Eisenberg D & Jucker M The amyloid state of proteins in human diseases. Cell 148, 1188–1203 (2012). [PubMed: 22424229]

2. Roberts AN et al. Molecular and functional characterization of amylin, a peptide associated with type 2 diabetes mellitus. Proc. Natl. Acad. Sci. U. S. A. 86, 9662–9666 (1989). [PubMed: 2690069]
3. Westermark P Amyloid in the islets of Langerhans: thoughts and some historical aspects. Ups. J. Med. Sci. 116, 81–89 (2011). [PubMed: 21486192]
4. Westermark P et al. Amyloid fibrils in human insulinoma and islets of Langerhans of the diabetic cat are derived from a neuropeptide-like protein also present in normal islet cells. Proc. Natl. Acad. Sci. U. S. A. 84, 3881–3885 (1987). [PubMed: 3035556]
5. Cooper GJ et al. Amylin found in amyloid deposits in human type 2 diabetes mellitus may be a hormone that regulates glycogen metabolism in skeletal muscle. Proc. Natl. Acad. Sci. U. S. A. 85, 7763–7766 (1988). [PubMed: 3051005]
6. Höppener JW, Ahrén B & Lips CJ Islet amyloid and type 2 diabetes mellitus. N. Engl. J. Med. 343, 411–419 (2000). [PubMed: 10933741]
7. Westermark P, Wernstedt C, Wilander E & Sletten K A novel peptide in the calcitonin gene related peptide family as an amyloid fibril protein in the endocrine pancreas. Biochem. Biophys. Res. Commun. 140, 827–831 (1986). [PubMed: 3535798]
8. Westermark GT, Gebre-Medhin S, Steiner DF & Westermark P Islet amyloid development in a mouse strain lacking endogenous islet amyloid polypeptide (IAPP) but expressing human IAPP. Mol. Med. Camb. Mass 6, 998–1007 (2000). [PubMed: 11474116]
9. Fernández-Alvarez J et al. Stable and functional regeneration of pancreatic beta-cell population in nSTZ-rats treated with tungstate. Diabetologia 47, 470–477 (2004). [PubMed: 14968293]
10. Pilkington EH et al. Pancreatic β-Cell Membrane Fluidity and Toxicity Induced by Human Islet Amyloid Polypeptide Species. Sci. Rep. 6, 21274 (2016). [PubMed: 26880502]
11. Mukherjee A et al. Induction of IAPP amyloid deposition and associated diabetic abnormalities by a prion-like mechanism. J. Exp. Med. 214, 2591–2610 (2017). [PubMed: 28765400]
12. Cao Q, Boyer DR, Sawaya MR, Ge P & Eisenberg DS Cryo-EM structure and inhibitor design of human IAPP (amylin) fibrils. Nat. Struct. Mol. Biol. (2020) doi:10.1038/s41594-020-0435-3.
13. Luca S, Yau W-M, Leapman R & Tycko R Peptide conformation and supramolecular organization in amylin fibrils: constraints from solid-state NMR. Biochemistry 46, 13505–13522 (2007). [PubMed: 17979302]
14. Bedrood S et al. Fibril Structure of Human Islet Amyloid Polypeptide. J. Biol. Chem. 287, 5235–5241 (2012). [PubMed: 22187437]
15. Röder C et al. Cryo-EM structure of islet amyloid polypeptide fibrils reveals similarities with amyloid-β fibrils. Nat. Struct. Mol. Biol. 27, 660–667 (2020). [PubMed: 32541895]
16. Gallardo R et al. Fibril structures of diabetes-related amylin variants reveal a basis for surface-templated assembly. Nat. Struct. Mol. Biol. (2020) doi:10.1038/s41594-020-0496-3.
17. Zhang W et al. Heparin-induced tau filaments are polymorphic and differ from those in Alzheimer's and Pick's diseases. eLife 8, e43584 (2019). [PubMed: 30720432]
18. Schweighauser M et al. Structures of α-synuclein filaments from multiple system atrophy. Nature 585, 464–469 (2020). [PubMed: 32461689]
19. Scheres SHW Amyloid structure determination in RELION-3.1. Acta Crystallogr. Sect. Struct. Biol. 76, 94–101 (2020).
20. Chen M-S et al. Characterizing the assembly behaviors of human amylin: a perspective derived from C-terminal variants. Chem. Commun. Camb. Engl. 49, 1799–1801 (2013).
21. Sakagashira S et al. Missense Mutation of Amylin Gene (S20G) in Japanese NIDDM Patients. Diabetes 45, 1279–1281 (1996). [PubMed: 8772735]
22. Meier DT et al. The S20G substitution in hIAPP is more amyloidogenic and cytotoxic than wild-type hIAPP in mouse islets. Diabetologia 59, 2166–2171 (2016). [PubMed: 27393137]
23. Sakagashira S et al. S20G mutant amylin exhibits increased in vitro amyloidogenicity and increased intracellular cytotoxicity compared to wild-type amylin. Am. J. Pathol. 157, 2101–2109 (2000). [PubMed: 11106582]
24. Cao P et al. Sensitivity of amyloid formation by human islet amyloid polypeptide to mutations at residue 20. J. Mol. Biol. 421, 282–295 (2012). [PubMed: 22206987]

25. Janson J et al. Increased risk of type 2 diabetes in Alzheimer disease. Diabetes 53, 474–481 (2004). [PubMed: 14747300]
26. Miklossy J et al. Beta amyloid and hyperphosphorylated tau deposits in the pancreas in type 2 diabetes. Neurobiol. Aging 31, 1503–1515 (2010). [PubMed: 18950899]
27. Peila R, Rodriguez BL, Launer LJ, & Honolulu-Asia Aging Study. Type 2 diabetes, APOE gene, and the risk for dementia and related pathologies: The Honolulu-Asia Aging Study. Diabetes 51, 1256–1262 (2002). [PubMed: 11916953]
28. Oskarsson ME et al. In vivo seeding and cross-seeding of localized amyloidosis: a molecular link between type 2 diabetes and Alzheimer disease. Am. J. Pathol. 185, 834–846 (2015). [PubMed: 25700985]
29. Moreno-Gonzalez I et al. Molecular interaction between type 2 diabetes and Alzheimer's disease through cross-seeding of protein misfolding. Mol. Psychiatry 22, 1327–1334 (2017). [PubMed: 28044060]
30. O'Nuallain B, Williams AD, Westermark P & Wetzel R Seeding specificity in amyloid growth induced by heterologous fibrils. J. Biol. Chem. 279, 17490–17499 (2004). [PubMed: 14752113]
31. Krotee P et al. Common fibrillar spines of amyloid-β and human islet amyloid polypeptide revealed by microelectron diffraction and structure-based inhibitors. J. Biol. Chem. 293, 2888–2902 (2018). [PubMed: 29282295]
32. Andreetto E et al. A Hot-Segment-Based Approach for the Design of Cross-Amyloid Interaction Surface Mimics as Inhibitors of Amyloid Self-Assembly. Angew. Chem. Int. Ed Engl. 54, 13095–13100 (2015). [PubMed: 26336938]
33. Lövestam S et al. Seeded assembly in vitro does not replicate the structures of α-synuclein filaments from multiple system atrophy. FEBS Open Bio (2021) doi:10.1002/2211-5463.13110.
34. Fujiwara H et al. alpha-Synuclein is phosphorylated in synucleinopathy lesions. Nat. Cell Biol. 4, 160–164 (2002). [PubMed: 11813001]
35. Sorrentino ZA & Giasson BI The emerging role of α-synuclein truncation in aggregation and disease. J. Biol. Chem. 295, 10224–10244 (2020). [PubMed: 32424039]
36. Asthana S, Mallick B, Alexandrescu AT & Jha S IAPP in type II diabetes: Basic research on structure, molecular interactions, and disease mechanisms suggests potential intervention strategies. Biochim. Biophys. Acta BBA - Biomembr. 1860, 1765–1782 (2018).
37. Jurgens CA et al. β-cell loss and β-cell apoptosis in human type 2 diabetes are related to islet amyloid deposition. Am. J. Pathol. 178, 2632–2640 (2011). [PubMed: 21641386]
38. Krotee P et al. Atomic structures of fibrillar segments of hIAPP suggest tightly mated β-sheets are important for cytotoxicity. eLife 6, (2017).
39. Falcon B et al. Tau filaments from multiple cases of sporadic and inherited Alzheimer's disease adopt a common fold. Acta Neuropathol. (Berl.) 136, 699–708 (2018). [PubMed: 30276465]
40. Falcon B et al. Novel tau filament fold in chronic traumatic encephalopathy encloses hydrophobic molecules. Nature 568, 420–423 (2019). [PubMed: 30894745]
41. Zhang W et al. Novel tau filament fold in corticobasal degeneration. Nature 580, 283–287 (2020). [PubMed: 32050258]
42. Boyer DR et al. Structures of fibrils formed by α-synuclein hereditary disease mutant H50Q reveal new polymorphs. Nat. Struct. Mol. Biol. 26, 1044–1052 (2019). [PubMed: 31695184]
43. Johnson KH et al. Feline insular amyloid: immunohistochemical and immunochemical evidence that the amyloid is insulin-related. Vet. Pathol. 22, 463–468 (1985). [PubMed: 3901495]
44. Mastronarde DN Automated electron microscope tomography using robust prediction of specimen movements. J. Struct. Biol. 152, 36–51 (2005). [PubMed: 16182563]
45. Grant T & Grigorieff N Automatic estimation and correction of anisotropic magnification distortion in electron microscopes. J. Struct. Biol. 192, 204–208 (2015). [PubMed: 26278979]
46. Rohou A & Grigorieff N CTFFIND4: Fast and accurate defocus estimation from electron micrographs. J. Struct. Biol. 192, 216–221 (2015). [PubMed: 26278980]
47. Grant T & Grigorieff N Measuring the optimal exposure for single particle cryo-EM using a 2.6 Å reconstruction of rotavirus VP6. eLife 4, e06980 (2015). [PubMed: 26023829]

48. Tang G et al. EMAN2: an extensible image processing suite for electron microscopy. J. Struct. Biol. 157, 38–46 (2007). [PubMed: 16859925]
49. Wagner T et al. Two particle-picking procedures for filamentous proteins: SPHIRE-crYOLO filament mode and SPHIRE-STRIPER. Acta Crystallogr. Sect. Struct. Biol. 76, 613–620 (2020).
50. He S & Scheres SHW Helical reconstruction in RELION. J. Struct. Biol. 198, 163–176 (2017). [PubMed: 28193500]
51. Scheres SHW RELION: Implementation of a Bayesian approach to cryo-EM structure determination. J. Struct. Biol. 180, 519–530 (2012). [PubMed: 23000701]
52. Terwilliger TC, Sobolev OV, Afonine PV & Adams PD Automated map sharpening by maximization of detail and connectivity. Acta Crystallogr. Sect. Struct. Biol. 74, 545–559 (2018).
53. Emsley P, Lohkamp B, Scott WG & Cowtan K Features and development of Coot. Acta Crystallogr. D Biol. Crystallogr. 66, 486–501 (2010). [PubMed: 20383002]
54. Afonine PV et al. Real-space refinement in PHENIX for cryo-EM and crystallography. Acta Crystallogr. Sect. Struct. Biol. 74, 531–544 (2018).
55. Chen VB et al. MolProbity: all-atom structure validation for macromolecular crystallography. Acta Crystallogr. D Biol. Crystallogr. 66, 12–21 (2010). [PubMed: 20057044]
56. Schrodinger. The PyMOL Molecular Graphics System, Version 1.8. (2015).
57. Warmack RA et al. Structure of amyloid-beta (20–34) with Alzheimer's-associated isomerization at Asp23 reveals a distinct protofilament interface. Nat. Commun. 10, 3357 (2019). [PubMed: 31350392]
58. Lu J-X et al. Molecular structure of beta-amyloid fibrils in Alzheimer's disease brain tissue. Cell 154, 1257–1268 (2013). [PubMed: 24034249]
59. Schutz AK et al. Atomic-resolution three-dimensional structure of amyloid beta fibrils bearing the Osaka mutation. Angew. Chem. Int. Ed Engl. 54, 331–335 (2015). [PubMed: 25395337]
60. Colvin MT et al. Atomic Resolution Structure of Monomorphic Abeta42 Amyloid Fibrils. J. Am. Chem. Soc. 138, 9663–9674 (2016). [PubMed: 27355699]
61. Gremer L et al. Fibril structure of amyloid-β(1–42) by cryo–electron microscopy. Science 358, 116–119 (2017). [PubMed: 28882996]
62. Walti MA et al. Atomic-resolution structure of a disease-relevant Abeta(1–42) amyloid fibril. Proc. Natl. Acad. Sci. U. S. A. 113, E4976–4984 (2016). [PubMed: 27469165]
63. Xiao Y et al. Abeta(1–42) fibril structure illuminates self-recognition and replication of amyloid in Alzheimer's disease. Nat. Struct. Amp Mol. Biol. 22, 499–505 (2015).
64. Luhrs T et al. 3D structure of Alzheimer's amyloid-beta(1–42) fibrils. Proc. Natl. Acad. Sci. U. S. A. 102, 17342–17347 (2005). [PubMed: 16293696]
65. Paravastu AK, Leapman RD, Yau W-M & Tycko R Molecular structural basis for polymorphism in Alzheimer's beta-amyloid fibrils. Proc. Natl. Acad. Sci. U. S. A. 105, 18349–18354 (2008). [PubMed: 19015532]
66. Sgourakis NG, Yau W-M & Qiang W Modeling an in-register, parallel "iowa" abeta fibril structure using solid-state NMR data from labeled samples with rosetta. Struct. Lond. Engl. 1993 23, 216–227 (2015).
67. Kollmer M et al. Cryo-EM structure and polymorphism of Aβ amyloid fibrils purified from Alzheimer's brain tissue. Nat. Commun. 10, 4760 (2019). [PubMed: 31664019]

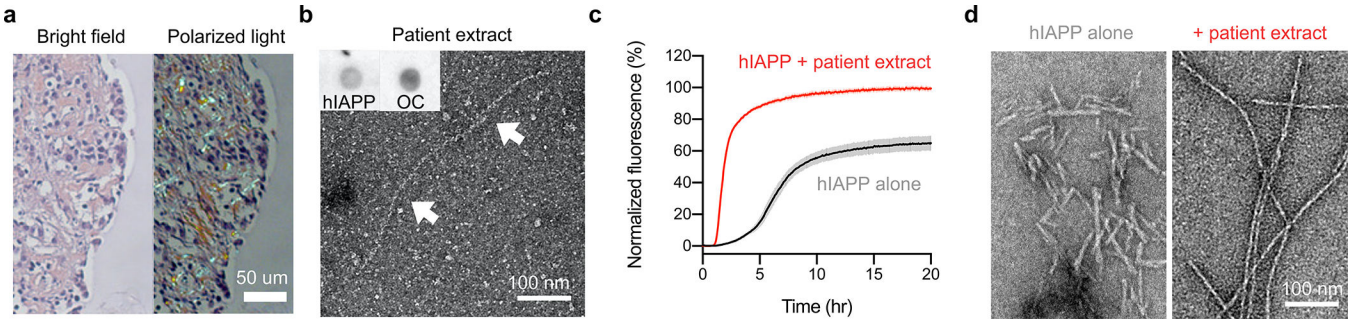

Fig. 1. Extraction of patient islet cells and seeding of fibril growth.

(A) Congo Red staining of a slice of islet cells from a donor with T2D (Case 6). **(B)** Negatively stained EM image of the elute-1 fraction in the immunoprecipitation assay; amyloid fibrils are indicated by arrows; the dot blots of the same fraction probed by anti-hIAPP (Amylin Polyclonal Antibody) and anti-amyloid fibrils OC antibodies are shown as inserts. **(C)** ThT aggregation curves of freshly prepared synthetic hIAPP peptide incubated with (red) and without (black) the patient extracted fibrils as fibril growth seeds. Data are shown as mean ± s.d., n=3 independent experiments. **(D)** Negatively stained EM images of same samples in (C) after 20 hours of incubation.

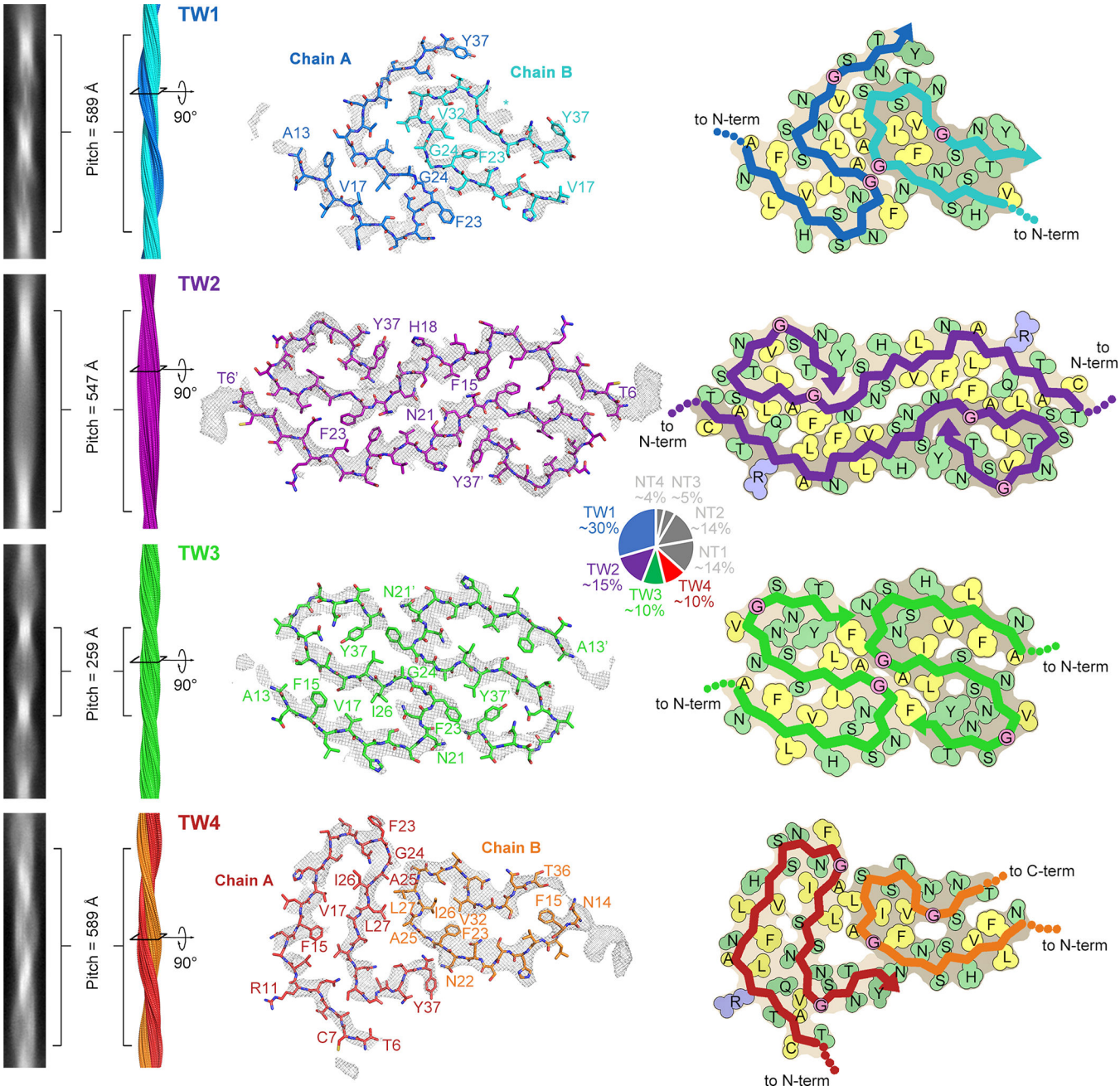

Fig. 2. Cryo-EM structures of patient-extract-seeded hIAPP fibrils.

Far left: representative 2D classes of four morphologies that display twisting features (TW1-TW4); middle left: fibril reconstructions of TW1-TW4 scaled to match 2D classes, the pitch of each morphology is labelled; middle right: density and atomic model of one cross-sectional layer of each morphology; far right: schematic model of each morphology, hydrophobic residues are colored in yellow, polar ones are colored in green, glycines are pink, and arginines are blue. N-term, N terminus; C-term, C terminus. Percentage of total helical segments belonging to each morphology shown by pie chart in the middle, and the numbers are calculated via 2D classification.

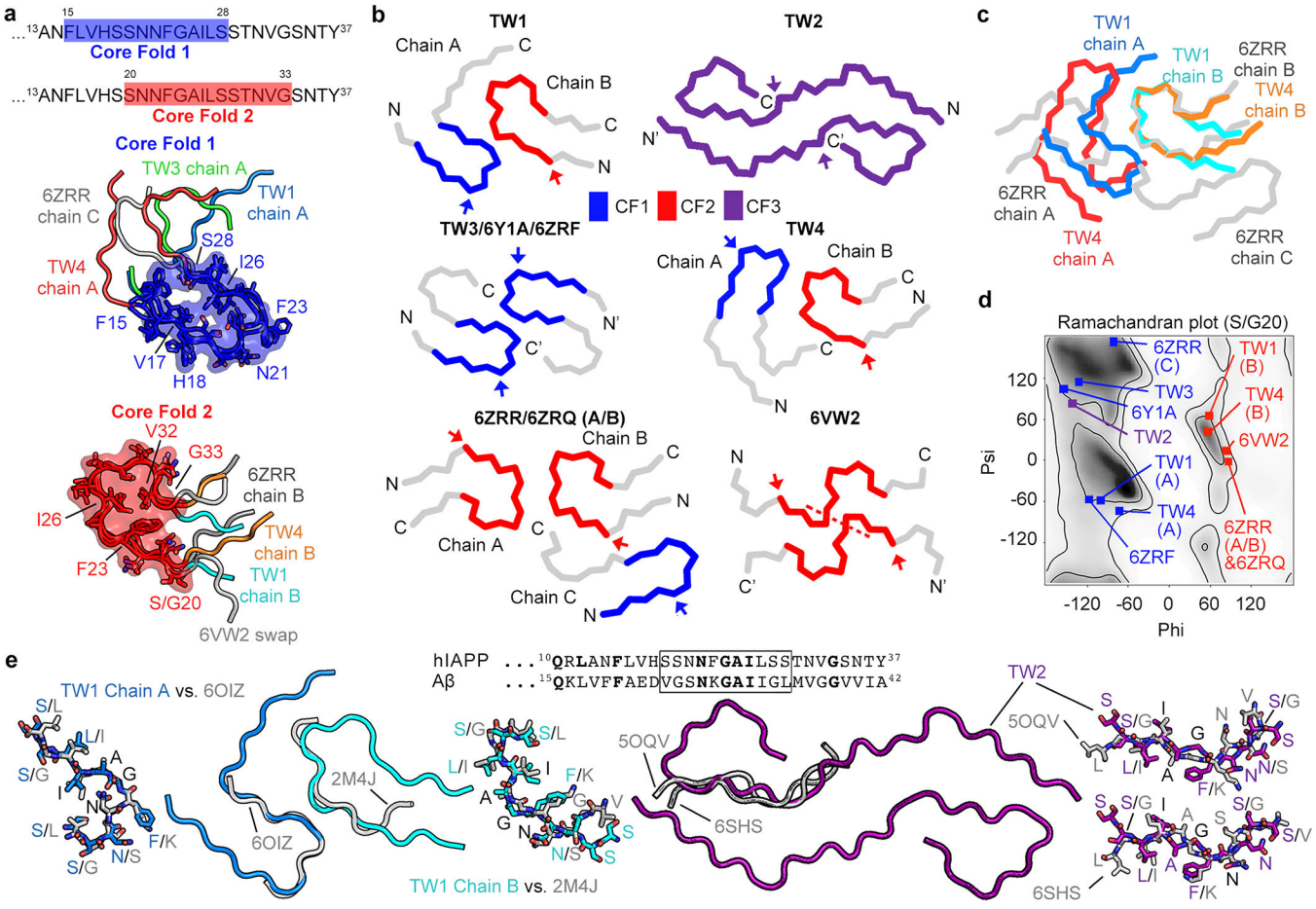

Fig. 3. Structural comparisons of hIAPP fibrils seeded with patient-extracted fibrils.

(A) Two conserved core folds (CF1 and CF2) in reported hIAPP fibril structures. Top: sequences of CF1 and CF2; bottom: superposition of hIAPP fibril folds that contain CF1 and CF2. **(B)** Six main chain views down fibril axes of selected hIAPP structures, CF1, CF2 and CF3 are blue, red and purple, respectively, and the rest of the main chains are gray. The arrows indicate the position of Ser20/Gly20. **(C)** Superposition of TW1, TW4 and 6ZRR aligned on their CF2 regions of chain B. **(D)** Ramachandran plot of position 20 of each hIAPP fibril structures, and color coded by CF1 (blue), CF2 (red) and CF3 (purple). **(E)** Structural alignments of TW1 (chain A, marine; chain B, cyan) and TW2 (purple) vs. Aβ fibril structures (gray, residue 24–34 are shown). Inset: sequence alignment of hIAPP and Aβ. The boxed regions are predicted to be responsible for cross-seeding, and the residues that are identical in hIAPP and Aβ are shown as bold. For superimposition details of panel A and E see Supplementary Table 2.

Table 1

Cryo-EM data collection, refinement and validation statistics

	TW1 (EMD-23686, PDB 7M61)	TW2 (EMD-23687, PDB 7M62)	TW3 (EMD-23688, PDB 7M64)	TW4 (EMD-23689, PDB 7M65)
Data collection and processing				
Magnification	×64,000	×64,000	×64,000	×64,000
Voltage (kV)	300	300	300	300
Electron exposure (e^{-}/Å^2)	45–85	45–85	45–85	45–85
Defocus range (μm)	0.7–2.7	0.7–2.7	0.7–2.7	0.7–2.7
Pixel size (Å)	1.055	1.055	1.055	1.055
Symmetry imposed	C_1	C_2	C_1	C_1
Helical rise (Å)	4.81	4.80	2.40	4.81
Helical twist (°)	−2.94	178.42	178.33	−2.94
Initial particle images (no.)	339,132	953,276	285,645	170,541
Final particle images (no.)	26,608	23,957	17,853	20,365
Map resolution (Å)	3.8	3.9	4.0	4.1
FSC threshold	0.143	0.143	0.143	0.143
Map resolution range (Å)	200–3.8	200–3.9	200–4.0	200–4.1
Refinement				
Initial model used (PDB code)	De novo	De novo	6Y1A	De novo
Model resolution (Å)	3.7	4.1	4.0	4.0
FSC threshold	0.5	0.5	0.5	0.5
Model resolution range (Å)	200–3.7	200–4.1	200–4.0	200–4.0
Map sharpening *B* factor (Å^2)	83	98	155	100
Model composition				
Nonhydrogen atoms	1,690	2,380	1,850	2,025
Protein residues	230	320	250	275
Ligands	0	0	0	0
B factors (Å^2)				
Protein	45.8	150.3	67.7	92.4
Ligand	-	-	-	-
R.m.s. deviations				
Bond lengths (Å)	0.007	0.007	0.008	0.009
Bond angles (°)	1.166	1.126	1.150	1.506
Validation				
MolProbity score	2.51	2.78	2.30	2.70
Clashscore	23.6	32.8	19.5	31.1
Poor rotamers (%)	0	0	0	0
Ramachandran plot				
Favored (%)	85.71	76.67	91.3	82.35
Allowed (%)	14.29	23.33	8.7	17.65
Disallowed (%)	0	0	0	0

Table 2

Comparative solvation energy calculations

Fibril structure	Fibril information	Energy per layer (kcal/mol)	Energy per residue (kcal/mol)
TW1 (PDB7M61)	Synthetic wild-type hIAPP peptide seeded by patient extract	−24.4	−0.53 (chain A, −0.58; chain B, −0.48)
TW2 (PDB7M62)		−31.5	−0.49
TW3 (PDB7M64)		−27.0	−0.54
TW4 (PDB7M65)		−26.7	−0.49 (chain A, −0.49; chain B, −0.48)
6Y1A	Synthetic wild-type hIAPP peptide aggregated in vitro	−23.2	−0.46
6VW2	SUMO-tagged recombinant hIAPP aggregated in vitro	−21.6	−0.45
6ZRF	Synthetic wild-type hIAPP peptide aggregated in vitro	−24.0	−0.48
6ZRQ	Synthetic hIAPP S20G peptide	−25.1	−0.55
6ZRR	aggregated in vitro	−37.1	−0.54 (chain A, −0.53; chain B, −0.62; chain C, −0.46)